ADVANCED MATERIALS
www.advmat.de

Bulk-Rashba Effect with Suppressed Spin Relaxation in a Polar Phase of $Bi_{1-x}In_{1+x}O_3$

*Deokyoung Kang, Xue-Zeng Lu, Megha Acharya, Sajid Husain, Isaac Harris, Piush Behera, Ching-Che Lin, Ella Banyas, Alex Smith, Francesco Ricci, Menglin Zhu, Bridget R. Denzer, Tanguy Terlier, Shu Wang, Tae Yeon Kim, Lucas Caretta, Douglas Natelson, James M. LeBeau, Jeffrey B. Neaton, Ramamoorthy Ramesh, James M. Rondinelli, and Lane W. Martin**

The Rashba effect enables control over the spin degree of freedom, particularly in polar materials where the polar symmetry couples to Rashba-type spin splitting. The exploration of this effect, however, has been hindered by the scarcity of polar materials exhibiting the bulk-Rashba effect and rapid spin-relaxation effects dictated by the D'yakonov–Perel mechanism. Here, a polar $LiNbO_3$-type *R*3*c* phase of $Bi_{1-x}In_{1+x}O_3$ with $x \approx 0.15$–0.24 is stabilized via epitaxial growth, which exhibits a bulk-Rashba effect with suppressed spin relaxation as a result of its unidirectional spin texture. As compared to the previously observed non-polar *Pnma* phase, this polar phase exhibits higher conductivity, reduced bandgap, and enhanced dielectric and piezoelectric responses. Combining first-principles calculations and multimodal magnetotransport measurements, which reveal weak (anti)localization, anisotropic magnetoresistance, planar-Hall effect, and nonreciprocal charge transport, a bulk-Rashba effect without rapid spin relaxation is demonstrated. These findings offer insights into spin-orbit coupling physics within polar oxides and suggest potential spintronic applications.

1. Introduction

The interplay between the orbital and spin degrees of freedom, known as spin-orbit coupling (SOC), has been sought for use in low-power spintronics.[1–5] In particular, the Rashba effect, which arises from the SOC induced by broken inversion symmetry, has garnered attention as a way to generate, manipulate, and detect spin transport.[2,6–12] Although the Rashba effect has primarily been studied in 2D systems (e.g., GaAs-based quantum-wells[13–15] or $LaAlO_3/SrTiO_3$ heterointerfaces[9,16–19]), these systems typically exhibit relatively weak Rashba strengths as characterized by the Rashba coefficient $\alpha_R \approx 1$–10 meV Å. Additionally, spin-flip processes governed by the D'yakonov-Perel (DP) mechanism can lead to spin-relaxation,[20] compromising coherent control of the spin. Since

D. Kang, M. Acharya, S. Husain, P. Behera, C.-C. Lin, S. Wang
Department of Materials Science and Engineering
University of California, Berkeley
Berkeley, CA 94720, USA

D. Kang, C.-C. Lin, T. Y. Kim, R. Ramesh, L. W. Martin
Rice Advanced Materials Institute
Rice University
Houston, TX 77005, USA
E-mail: lwmartin@rice.edu

X.-Z. Lu, J. M. Rondinelli
Department of Materials Science and Engineering
Northwestern University
Evanston, IL 60208, USA

X.-Z. Lu
Key Laboratory of Quantum Materials and Devices of Ministry of Education
School of Physics
Southeast University
Nanjing 211189, China

The ORCID identification number(s) for the author(s) of this article can be found under https://doi.org/10.1002/adma.202504684

DOI: 10.1002/adma.202504684

M. Acharya, S. Husain, E. Banyas, S. Wang, J. B. Neaton
Materials Sciences Division
Lawrence Berkeley National Laboratory
Berkeley, CA 94720, USA

I. Harris, E. Banyas, A. Smith, F. Ricci, J. B. Neaton
Department of Physics
University of California
Berkeley, CA 94720, USA

F. Ricci
Université Catholique de Louvain (UCLouvain)
Institute of Condensed Matter and Nanosciences (IMCN)
Chemin des Étoiles 8, Louvain-la-Neuve B-1348, Belgium

M. Zhu, B. R. Denzer, J. M. LeBeau
Department of Materials Science and Engineering
Massachusetts Institute of Technology
Cambridge, MA, USA

T. Terlier
SIMS Laboratory
Shared Equipment Authority
Rice University
Houston, TX 77005, USA

the DP mechanism dictates that the spin-relaxation time (τ_S) is inversely proportional to the Rashba strength; there is a trade-off in obtaining high Rashba strength and long τ_S.[20–22] It has been demonstrated, however, that the manifestation of persistent-spin texture (PST) with a persistent-spin helix (PSH) spin-wave mode can suppress DP-spin relaxation by balancing the Rashba- and Dresselhaus-type SOC.[23–26] This approach necessitates fine control of film thickness and gate voltage; a low $\alpha_R \approx$ 1–10 meV·Å and long PSH wavelength (≈1–10 µm) in 2D Rashba systems further limits their potential for use in spintronics.[25,27,28]

The bulk-Rashba effect, on the other hand, manifests itself as a momentum-dependent spin splitting arising from the polar symmetry in three-dimensional crystals such as GeTe[8,11,29–33] and BiTeI,[6,34,35] which exhibit a higher α_R (≈ 1–5 eV Å) than typical 2D Rashba systems. Furthermore, theoretical works suggest that PST can also be realized by inducing unidirectional spin texture enforced by crystal symmetry,[36,37] where the PST can exhibit long $\tau_S \approx$ 1–10 ns even with higher values of $\alpha_R \approx$ 0.1–1 eV Å. There are a limited number of polar materials, however, that have been found to exhibit the bulk-Rashba effect, and experimental evidence for the bulk-Rashba effect with unidirectional spin texture remains elusive.[37,38]

Here, a previously unreported polar phase of $Bi_{1-x}In_{1+x}O_3$, exhibiting a $LiNbO_3$-type $R3c$ phase (henceforth R-$Bi_{1-x}In_{1+x}O_3$), is stabilized, which exhibits a bulk-Rashba effect with suppressed spin relaxation. While previous theoretical studies reported the potential for PST in a polar-$Pna2_1$ version of $BiInO_3$,[36] prior efforts had produced a non-polar-$Pnma$ version (henceforth O-$Bi_{1-x}In_{1+x}O_3$) in thin films.[39,40] Exploring a broader growth space using pulsed-laser deposition and epitaxial control, this work reveals a metastable, nonstoichiometric polar phase, R-$Bi_{1-x}In_{1+x}O_3$ (stabilized under a wide compositional range from $x \approx 0.15 - 0.34$). R-$Bi_{1-x}In_{1+x}O_3$ exhibits multiple twinned structural domains when films are grown on $DyScO_3$ $(110)_O$ substrates (henceforth (001)-oriented R-$Bi_{1-x}In_{1+x}O_3$) and with a monodomain structure when grown on $SrTiO_3$ (111) substrates (henceforth (111)-oriented R-$Bi_{1-x}In_{1+x}O_3$). As compared to O-$Bi_{1-x}In_{1+x}O_3$ films, R-$Bi_{1-x}In_{1+x}O_3$ films showed higher electrical conductivity due to a slightly reduced optical band gap and enhanced dielectric and piezoelectric responses corresponding to their polar nature. First-principles density-functional theory (DFT) calculations explore the structural stability of R-$Bi_{1-x}In_{1+x}O_3$ and reveal Rashba-type spin splitting with unidirectional spin texture when the Fermi level (E_F) exceeds no more than 3 meV above the conduction band minimum energy (E_{CBM}). R-$Bi_{1-x}In_{1+x}O_3$ films were systematically annealed in slightly oxygen-deficient environments to create oxygen vacancies such that the carrier concentration was tuned to access the potential unidirectional spin texture (i.e., E_F-$E_{CBM} < 3$ meV) and so that the films were adequately conductive for transport measurements. While weak antilocalization (WAL) with spin relaxation was observed in annealed multidomain (001)-oriented R-$Bi_{1-x}In_{1+x}O_3$ films, weak localization (WL) with a long $\tau_S > 3.36$ ns was observed in annealed, monodomain (111)-oriented R-$Bi_{1-x}In_{1+x}O_3$ films. Additional transport measurements, including planar-Hall effect, anisotropic magnetoresistance, and nonreciprocal charge transport studies, were completed on the annealed (111)-oriented R-$Bi_{1-x}In_{1+x}O_3$ films and confirm the bulk-Rashba effect with $\alpha_R \approx$ 760 meV Å.

2. Results and Discussion

2.1. Stabilizing Polar R-$Bi_{1-x}In_{1+x}O_3$

2.1.1. Film Growth and Structural Characterization

To explore the possible structural phases of $Bi_{1-x}In_{1+x}O_3$, 100 nm-thick $Bi_{1-x}In_{1+x}O_3$ films were grown on multiple substrates (i.e., MgO (001), $DyScO_3$ $(110)_O$, and $SrTiO_3$ (111)) via pulsed-laser deposition (Experimental Section) using a 10% bismuth-excess target ($Bi_{1.1}InO_3$). In this work, O denotes orthorhombic indices and pc denotes pseudocubic indices. X-ray-diffraction studies (Experimental Section) reveal that singe-phase $(200)_O$-oriented O-$Bi_{1-x}In_{1+x}O_3$ films are grown on MgO (001) substrates in the growth temperature (T_g) window 550–650 °C (top, **Figure 1a**) (Note S1 and Figure S1, Supporting Information); consistent with previous studies.[39,40] When the films are grown on $DyScO_3$ $(110)_O$ substrates, however, Bi_2O_3 is the primary phase at T_g = 550 °C (Experimental Section). At T_g = 650 °C, a new diffraction peak (at ≈45.6°) was observed, which does not correspond to any of the diffraction conditions for O-$BiInO_3$ or commonly expected secondary phases (e.g., Bi_2O_3 and In_2O_3) (middle, Figure 1a). Time-of-flight secondary ion mass spectrometry (ToF-SIMS) measurements (Experimental Section) reveal that all films grown at T_g = 650 °C exhibit bismuth-loss ($x \approx$ 0.24–0.34) (Figure S2, Supporting Information) due to the relatively high volatility of bismuth. To compensate for bismuth-deficiency in the films grown at T_g = 650 °C, a 30% bismuth-excess target ($Bi_{1.3}InO_3$) was also used to grow films and it was found that, even in this case, while it was possible to partially mitigate bismuth loss, the films were still mildly bismuth-deficient ($x \approx$ 0.15) (Nots S1 and Figure S3, Supporting Information). These observations suggest that this new structural phase exhibits a wide

T. Y. Kim, R. Ramesh, L. W. Martin
Department of Materials Science and NanoEngineering
Rice University
Houston, TX 77005, USA
L. Caretta
School of Engineering
Brown University
Providence, RI 77005, USA
D. Natelson, R. Ramesh, L. W. Martin
Department of Physics and Astronomy
Rice University
Houston, TX 77005, USA
D. Natelson
Rice Center for Quantum Materials and Department of Electrical and Computer Engineering
Rice University
Houston, TX 77005, USA
J. B. Neaton
Kavli Energy NanoScience Institute at Berkeley
Berkeley, CA 94720, USA
L. W. Martin
Department of Chemistry
Rice University
Houston, TX 77005, USA

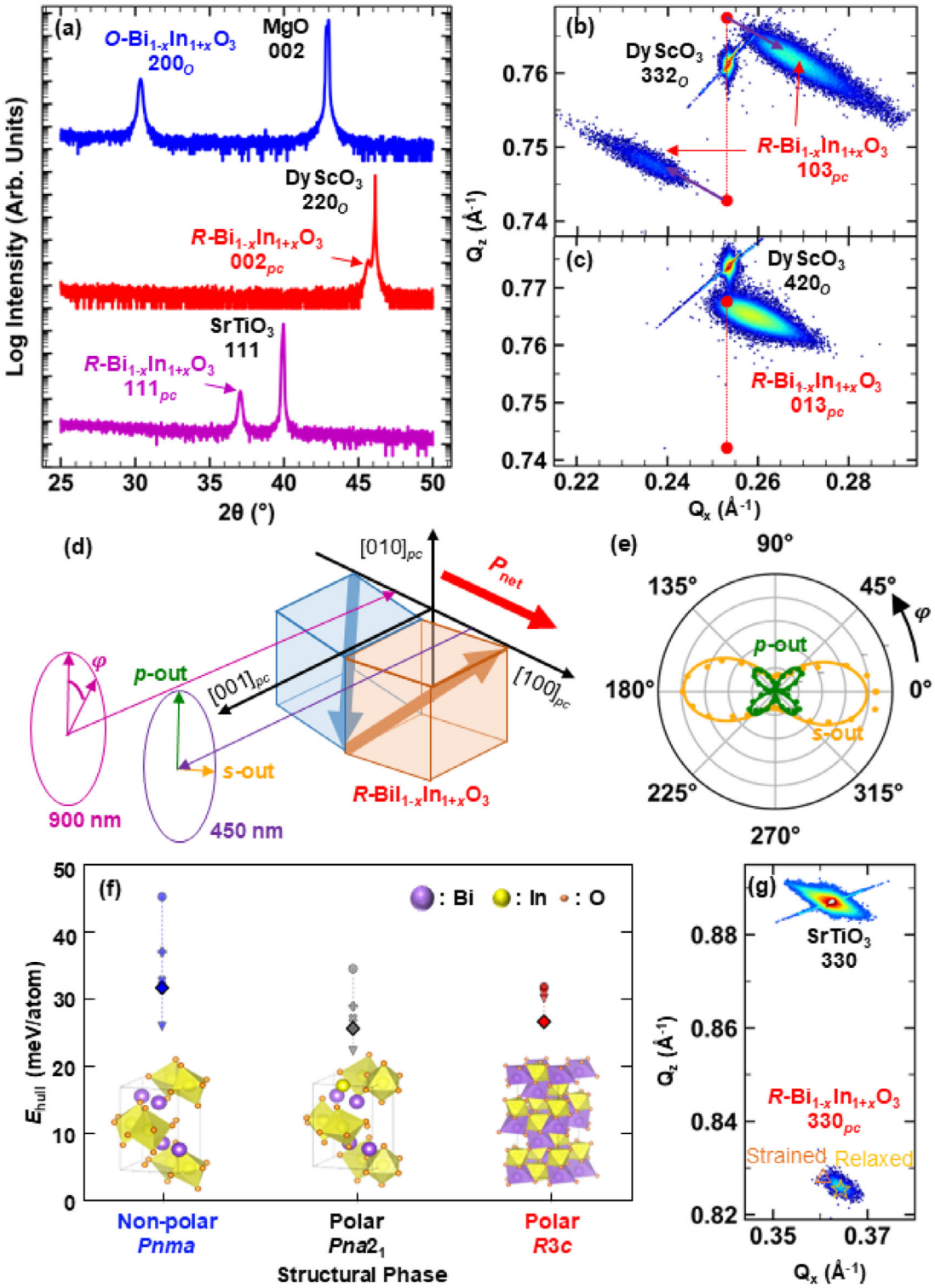

Figure 1. Structural analysis of the R-$Bi_{1-x}In_{1+x}O_3$ ($x \approx 0.24$–0.34) films. a) X-ray-diffraction measurements (θ-2θ line scans) of $BiInO_3$ films grown on (top-to-bottom) MgO (002), $DyScO_3$ (110)$_O$, and $SrTiO_3$ (111) substrates. X-ray reciprocal space maps of the (001)-oriented R-$Bi_{1-x}In_{1+x}O_3$ films about the b) 103$_{pc}$- and c) 013$_{pc}$-diffraction conditions. d) Schematic illustration of second harmonic generation (SHG) in transmission of (001)-oriented R-$Bi_{1-x}In_{1+x}O_3$ films. e) Yellow and green data points correspond to the SHG signal as a function of φ with s-out and p-out analyzer configurations, respectively. The solid lines are fitting curves. f) Calculated energy above hull (E_{hull}) and schematic crystal structure of different structural phases of $BiInO_3$, including a non-polar-*Pnma*, polar-*Pna*2$_1$, and polar-*R*3*c* phase. Each marker corresponds to a different exchange-correlation functional: diamonds are PBEsol, triangles are LDA, circles are PBE, pluses are r2SCAN, and Xs are SCAN. g) X-ray reciprocal space maps of (111)-oriented R-$Bi_{1-x}In_{1+x}O_3$ films grown on $SrTiO_3$ (111) substrates about the 330$_{pc}$-diffraction condition.

compositional range for stability (at least $x \approx 0.15–0.34$; Note S1, Supporting Information) and potentially suggests that a small loss of bismuth could be required to assure phase stability. Hereafter, $x \approx 0.24–0.34$ will refer to $Bi_{1-x}In_{1+x}O_3$ films grown at $T_g = 650$ °C using a $Bi_{1.1}InO_3$ target. The $Bi_{1-x}In_{1+x}O_3$ films could be reproducibly grown on $DyScO_3$ $(110)_O$ substrates under the same growth conditions (i.e., $T_g = 650$ °C, $Bi_{1.1}InO_3$ target; Figure S4, Supporting Information).

To understand the crystal structure of this new structural phase of the $Bi_{1-x}In_{1+x}O_3$ films grown on $DyScO_3$ $(110)_O$ substrates, reciprocal space mapping (RSM) studies (Experimental Section) were conducted about the 220_O-diffraction peak of $DyScO_3$, and reveal that the films exhibit two structural variants with a crystallographic tilt of ±1.25° (0.57°) along the $[100]_{pc}$ ($[010]_{pc}$) (Figure S5, Supporting Information). Further asymmetric RSM studies reveal that the two structural variants exhibit a shear distortion with structural distortion angle $\beta \approx 3.98°$ along the $[1\bar{1}0]_{pc}$ and $[\bar{1}\bar{1}0]_{pc}$, respectively, as evidenced by the two vertically separated diffraction peaks near the 332_O-diffraction condition of $DyScO_3$ (110) (Figure 1b) and one diffraction peak near the 420_O-diffraction condition of $DyScO_3$ $(110)_O$ (Figure 1c) (Note S2, Supporting Information). Such RSM studies resemble those for $BiFeO_3$ films,[41] suggesting that the films exhibit a rhombohedral-like structure. The value of $\beta \approx 3.98°$ is, however, unusually large for a perovskite structure (typically $\beta \approx 0.1–0.8°$),[42] and suggests that the $Bi_{1-x}In_{1+x}O_3$ films likely form a non-perovskite rhombohedral, corundum-derivative structure (i.e., ilmenite-type $R\bar{3}c$ phase if non-polar and $LiNbO_3$-type $R3c$ phase if polar)[43–45] with lattice parameters $a_H = 5.483$ Å and $c_H = 14.44$ Å (where H refers to a hexagonal symmetry), which are equivalent to $a_{pc} = 3.976$ Å with $\beta = 3.98°$. To differentiate between the non-polar and polar structures, second-harmonic-generation (SHG) studies (Experimental Section) were completed and reveal that the $Bi_{1-x}In_{1+x}O_3$ films are polar and, therefore, likely adopt the $LiNbO_3$-type $R3c$ structure with polarization along the $<111>_{pc}$ (Figure 1d,e). Furthermore, the symmetry of the polar plot aligns with the twinned domain structure which follows the point group symmetry m with the mirror plane $(x,0,z)_{pc}$ (Figure 1e) (Note S3, Supporting Information). Overall, the $Bi_{1-x}In_{1+x}O_3$ films grown on $DyScO_3$ $(110)_O$ substrates exhibit a twinned-domain structure wherein the two domain variants are a polar $LiNbO_3$-type phase with polarization along the $<111>_{pc}$. Henceforth, such films will be referred to as (001)-oriented R-$Bi_{1-x}In_{1+x}O_3$ films.

DFT calculations (Experimental Section) were performed to explore the stability of the R-$Bi_{1-x}In_{1+x}O_3$ phase with $x = 0–1$. R-$BiInO_3$ (i.e., $x = 0$) is found to be energetically competitive with the orthorhombic (non-polar-$Pnma$ and polar-$Pna2_1$) $BiInO_3$ phases ($E_{hull,Pnma} \approx 32$ meV · atom^{-1}, $E_{hull,Pna2_1} \approx 26$ meV · atom^{-1}, and $E_{hull,R3c} \approx 27$ meV · atom^{-1}), when computed using the PBEsol exchange-correlation functional (Figure 1f). Furthermore, the computed formation energies of these phases lie within 5 meV · atom^{-1} of each other for the majority of other exchange-correlation functionals tested (Figure S6, Supporting Information). Furthermore, the energy above the hull exhibits a small increase of only ≈20 meV · atom^{-1} as x is increased from 0 to 0.5, indicating that the bismuth-deficient phases are also energetically similar to the pristine phase (Note S4 and Figure S7, Supporting Information). Thus, it is posited that the R-$Bi_{1-x}In_{1+x}O_3$ phase is a viable polymorph to be found and that the bismuth loss in R-$Bi_{1-x}In_{1+x}O_3$ contributes to breaking this (effective) energetic stalemate—effectively lowering the tolerance factor and, therefore, stabilizing the $LiNbO_3$-type phase; effects commonly observed in other $LiNbO_3$-type phases.[43–45] Additionally, polar R-$BiInO_3$ exhibits a formation energy that is 108.8 meV · atom^{-1} lower than a corresponding centrosymmetric-$R\bar{3}c$ phase, and is predicted to have a spontaneous polarization of ≈101.9 μC cm^{-2} along the $[111]_{pc}$ suggesting the potential for a robustly polar phase.

To further understand how epitaxial growth impacts the phase stabilization, $Bi_{1-x}In_{1+x}O_3$ films were deposited on multiple substrates, revealing that R-$Bi_{1-x}In_{1+x}O_3$ can be stabilized over O-$Bi_{1-x}In_{1+x}O_3$ by selecting the appropriate substrate with a relative low lattice mismatch ($|\delta| \lesssim 1.78\%$) (Note S5 and Figure S8, Supporting Information) and adjusting the growth speed (Figure S9, Supporting Information). Of particular interest is growth on $SrTiO_3$ (111) substrates, which results in single-crystalline R-$Bi_{1-x}In_{1+x}O_3$ films with significantly improved crystalline quality (Note S6 and Figure S10, Supporting Information)—likely the result of eliminating crystallographic tilt and the twinned-domain structure (Figure 1a, bottom and g). Henceforth, $Bi_{1-x}In_{1+x}O_3$ films grown on $SrTiO_3$ (111) substrates will be referred to as (111)-oriented R-$Bi_{1-x}In_{1+x}O_3$ films. All told, a novel polar R-$Bi_{1-x}In_{1+x}O_3$ ($x \approx 0.15 - 0.34$) phase has been stabilized via epitaxial control, where single-crystalline films with high crystalline-quality can be obtained.

2.1.2. Electrical, Optical, Dielectric, and Piezoelectric Properties

Stabilization of the R-$Bi_{1-x}In_{1+x}O_3$ phase motivates the investigation of the electrical, optical, dielectric, and piezoelectric properties of both the (001)- and (111)-oriented R-$Bi_{1-x}In_{1+x}O_3$ films in comparison to O-$Bi_{1-x}In_{1+x}O_3$ films. First, leakage current density-electric field (J–E) curves (Experimental Section) measured along the in-plane direction reveal that both the (001)- and (111)-oriented R-$Bi_{1-x}In_{1+x}O_3$ films exhibit, in the as-grown state, a conductivity 10^2–10^3-times higher than that of the O-$Bi_{1-x}In_{1+x}O_3$ films (**Figure 2a**). This enhanced conductivity is found irrespective of the substrate upon which the R-$Bi_{1-x}In_{1+x}O_3$ films are grown (Note S7 and Figure S11, Supporting Information). Transmission geometry ultraviolet-visible-light spectroscopy (Experimental Section) helps explain this observation in that it reveals a reduced direct optical bandgap for R-$Bi_{1-x}In_{1+x}O_3$ (3.7 eV) as compared to O-$Bi_{1-x}In_{1+x}O_3$ (4.7 eV) (Figure 2b). Moreover, differences in the grown-in defect concentration (e.g., bismuth vacancies, oxygen vacancies, etc.) may also play a role in accounting for the enhanced conductivity in the R-$Bi_{1-x}In_{1+x}O_3$ films (Note S7 and Figure S12, Supporting Information).

In turn, the dielectric constant and loss (Experimental Section) were studied along the out-of-plane $[001]_{pc}$ for 100 nm-thick O-$Bi_{1-x}In_{1+x}O_3$ and (001)- and (111)-oriented R-$Bi_{1-x}In_{1+x}O_3$ films grown epitaxially with $La_{0.67}Sr_{0.33}MnO_3$ layers as the bottom and top electrodes (Figure 2c) (Experimental Section). The O-$Bi_{1-x}In_{1+x}O_3$ films exhibit a dielectric constant of ≈45, close to the O-$BiInO_3$ films reported previously.[39] The (111)-oriented R-$Bi_{1-x}In_{1+x}O_3$ films exhibit a slightly smaller dielectric constant of ≈40, a value consistent with other $LiNbO_3$-type materials,[46,47]

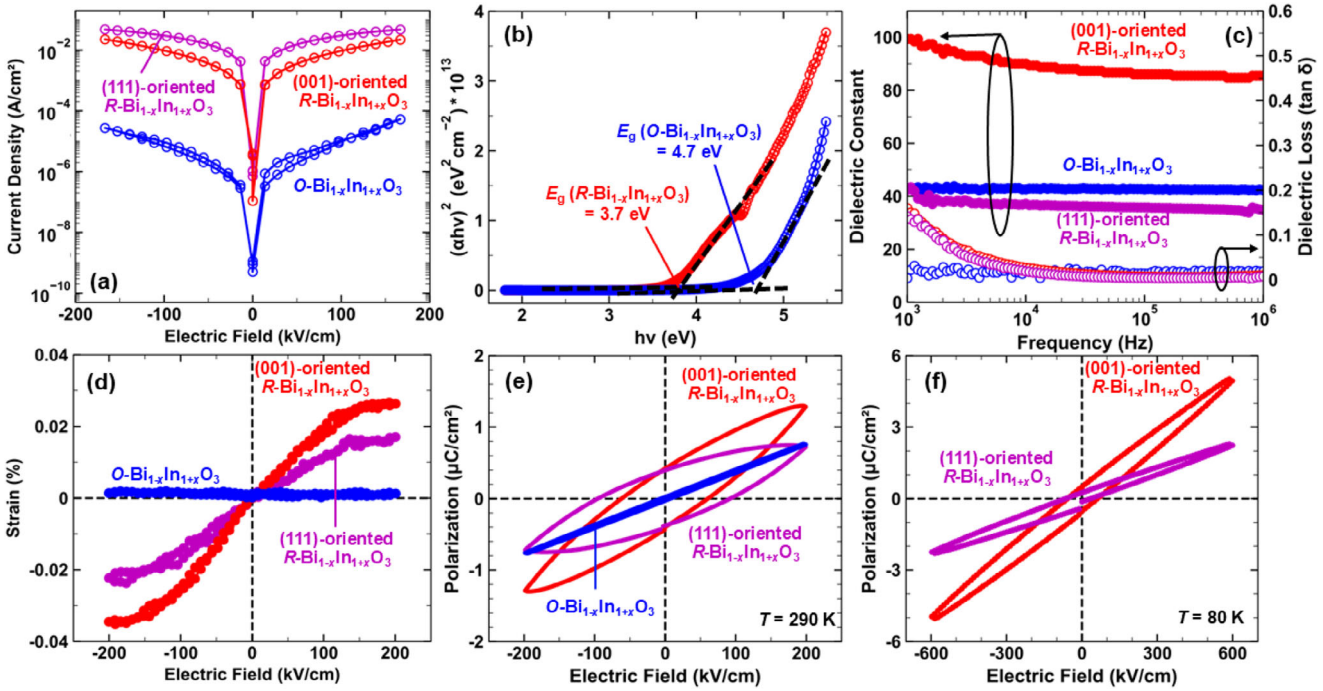

Figure 2. (Die)electric, optical, and electromechanical properties of $Bi_{1-x}In_{1+x}O_3$ ($x \approx 0.24$–0.34) films. a) Current density-electric field (J–E) curves of (001)- and (111)-oriented R-$Bi_{1-x}In_{1+x}O_3$ and O-$Bi_{1-x}In_{1+x}O_3$ films. b) Tauc plot showing the optical bandgap of the (001)-oriented R-$Bi_{1-x}In_{1+x}O_3$ and O-$Bi_{1-x}In_{1+x}O_3$ films. c) Frequency-dependent dielectric constant and dielectric loss of O-$Bi_{1-x}In_{1+x}O_3$ and (001)- and (111)-oriented R-$Bi_{1-x}In_{1+x}O_3$ films. d) Electromechanical strain of the same devices wherein the R-$Bi_{1-x}In_{1+x}O_3$ films exhibit a converse piezoelectric effect. Polarization versus electric field of the same devices as measured at e) 290 and f) 80 K, showing lossy and essentially linear dielectric behavior in the R-$Bi_{1-x}In_{1+x}O_3$ films.

while the (001)-oriented R-$Bi_{1-x}In_{1+x}O_3$ films exhibit a higher dielectric constant of ≈90 (at 10 kHz), possibly due to additional contribution from the domain walls[48] and polarization rotation (since the polarization could rotate from along the $[111]_{pc}$ toward the applied electric-field direction $[001]_{pc}$). All films studied in this work reveal low dielectric loss ($\tan\delta < 0.1$), but the R-$Bi_{1-x}In_{1+x}O_3$ films exhibited relatively higher dielectric loss than the O-$Bi_{1-x}In_{1+x}O_3$ films, consistent with the higher leakage currents. Furthermore, a small piezoelectric response was observed in the R-$Bi_{1-x}In_{1+x}O_3$ films (Figure 2d) via electromechanical measurements conducted on all the films using laser Doppler vibrometry[49] (Experimental Section). Although the O-$Bi_{1-x}In_{1+x}O_3$ films exhibited a negligible electromechanical response, showing an electromechanical strain (ε) of ≈0.001% at electric field $E = \pm 200$ kV cm^{-1} (likely arising only from electrostriction), the R-$Bi_{1-x}In_{1+x}O_3$ films showed an antisymmetric converse piezoelectric response with ε ≈ 0.02–0.03% at $E = \pm 200$ kV cm^{-1}. Similar to the dielectric response, a slightly increased piezoelectric response in the (001)-oriented R-$Bi_{1-x}In_{1+x}O_3$ films can be attributed to the polarization alignment therein such that the (001)-oriented R-$Bi_{1-x}In_{1+x}O_3$ films benefit from an additional contribution from the rotation of the polarization from along the $[111]_{pc}$ toward the $[001]_{pc}$.

The results thus far then beg the question as to if the R-$Bi_{1-x}In_{1+x}O_3$ films possess switchable spontaneous polarization (i.e., are ferroelectric) and thus attempts were made to switch the polarization with applied electric fields. Polarization-electric field loops (Experimental Section) reveal linear and slightly lossy dielectric behavior at room temperature *without* evidence of ferroelectric polarization switching for all $Bi_{1-x}In_{1+x}O_3$ heterostructures (Figure 2e); again, with (001)- and (111)-oriented R-$Bi_{1-x}In_{1+x}O_3$ films showing slightly more lossy behavior, consistent with the higher leakage currents. To further mitigate the effects of leakage, polarization-electric field hysteresis loops were also measured at 80 K, and again, there was no signature of ferroelectric switching for both out-of-plane (Figure 2f) and in-plane $[100]_{pc}$ measurements (Note S8 and Figure S13, Supporting Information). The lack of switching is likely due to a combination of high leakage currents, defects, and/or a high energy barrier for polarization switching. While polarization switching might be possible with improved film quality and reduced leakage, considering that the R-$Bi_{1-x}In_{1+x}O_3$ films remained non-switchable under 1.2 MV cm^{-1} at 80 K – well above the typical coercive field of most oxide ferroelectrics – suggests that the switching would be unlikely. All told, the electromechanical studies suggest that the R-$Bi_{1-x}In_{1+x}O_3$ films are piezoelectric, and while SHG studies also show that the R-$Bi_{1-x}In_{1+x}O_3$ films are polar, the absence of polarization switching prohibits referring to this phase as ferroelectric at this time.

2.2. Probing the Bulk-Rashba Effect in R–$Bi_{1-x}In_{1+x}O_3$

2.2.1. DFT Calculations and Transport Studies

Since R-$Bi_{1-x}In_{1+x}O_3$ exhibits polar symmetry, a sufficient condition for the manifestation of a bulk-Rashba effect, DFT calculations (Experimental Section) were conducted on R-$Bi_{1-x}In_{1+x}O_3$

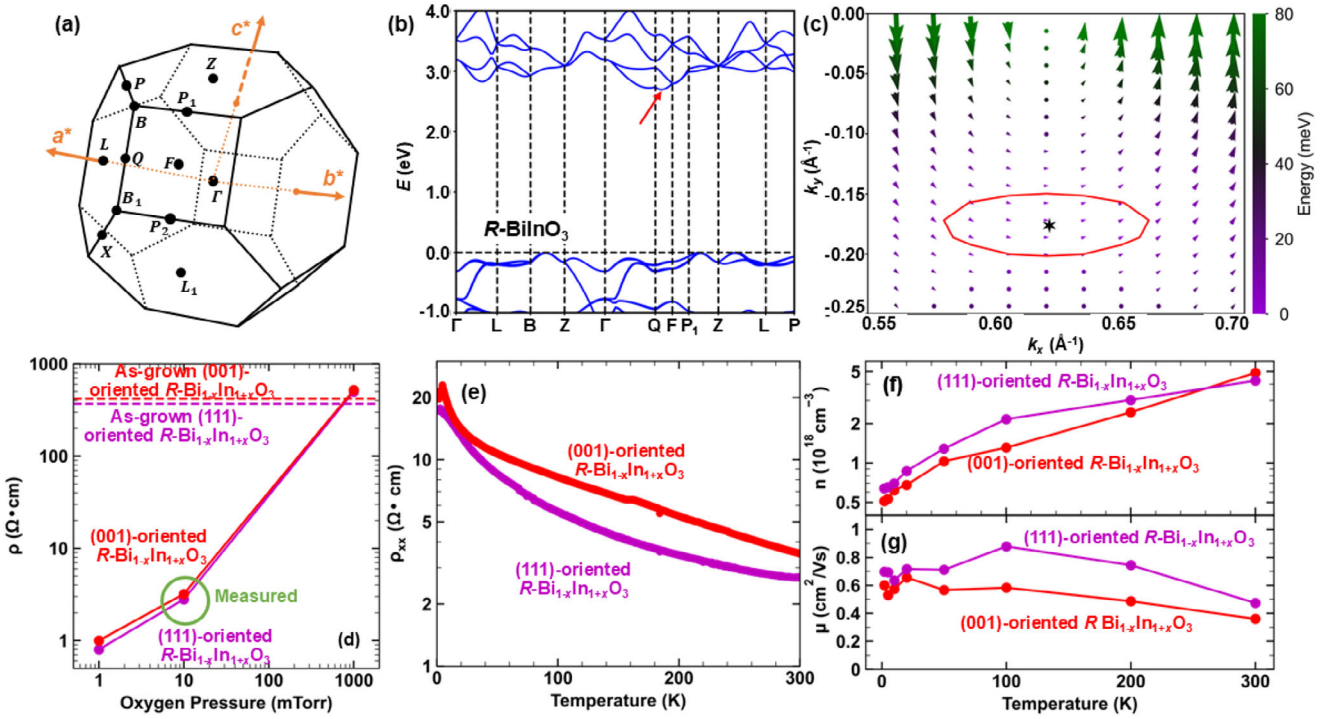

Figure 3. First-principles calculations and transport studies of R-$Bi_{1-x}In_{1+x}O_3$ ($x \approx 0.24$–0.34) films. a) Brillouin zone of the rhombohedral cell with reciprocal lattice vectors (a^*, b^*, c^*). b) Relativistic electronic band structure of R-$BiInO_3$, where the energy is given for the valence band maximum (VBM). The red arrow indicates the region where the spin texture is calculated. c) Spin textures about the lowest conduction band along the Q–F path projected on the k_x–k_y plane. Cartesian axes are defined as [11$\bar{1}$] for x, [1$\bar{1}$0] for y, and [111] for z with directions specified in the trigonal cell. The area enclosed by the solid red line indicates the region where the spin deviation is below (5°, 5°). The black star is the conduction band minimum (CBM). d) Resistivity of the (001)- and (111)-oriented R-$Bi_{1-x}In_{1+x}O_3$ films as a function of the oxygen pressure during annealing. The dashed line indicates the resistivity of the as-grown samples before annealing. The circled samples are further used for the later transport measurements. e) Resistivity (ρ_{xx}), f) carrier density (n), and (g) mobility (μ) of the (001)- and (111)-oriented R-$Bi_{1-x}In_{1+x}O_3$ films as a function of temperature.

($x = 0$ and 0.25) to probe the electronic structure and the spin textures. The primitive structure, in reciprocal space, is presented (**Figure** 3a) along with the unit cell of the crystal structure in real space (Figure S14, Supporting Information). The calculated band structure of R-$BiInO_3$ reveals a spin splitting due to the Rashba effect with the conduction band minimum (CBM) around the Q–F path (Figure 3b). Furthermore, a unidirectional spin texture, where the deviation angles (θ_x, θ_y) away from the spin direction at the CBM are less than (5°, 5°), was observed around the CBM when $E_F < 3$ meV (equivalently when the electron-carrier density $n < 1.2 \times 10^{18}$ cm^{-3}), revealing the potential for PST in R-$BiInO_3$ (Figure 3c). To further calculate the τ_S based on the PST, a $\boldsymbol{k}\cdot\boldsymbol{p}$ model was developed (Experimental Section) for the Q-F path along k_y, where there is no symmetry, and perpendicular to k_y where a mirror symmetry is present (Figure S14, Supporting Information). Notably, the $k \cdot p$ model can be built around any k_0 point with a specified point-group symmetry. As the CBM is in the Q-F path, where any k point has C_s symmetry, the $k \cdot p$ model can then be formulated according to the C_s symmetry. Typically, the $k \cdot p$ model should be derived around k_0 with a small Δk away from k_0. Since Γ is far away from the CBM, k_0 in the Q-F path was chosen for building the $k \cdot p$ model. As noted, mirror symmetries are critical to forming a PST. In ferroelectric compounds, which often exhibit C_{2v} point group symmetry, PSTs are typically stabilized by mirror symmetries along specific momentum-space directions. These symmetry-enforced configurations are referred to as Type-I PSTs, or symmetry-protected PSTs. In contrast, the strength of SOC parameters can produce an accidental or Type-II PST that is not enforced by symmetry but rather assisted by it[3] . In polar crystals, for instance, an accidental PST can emerge even in the absence of mirror symmetry. Its stability is governed by the relative strength of SOC along two orthogonal momentum directions within the plane of the PST—typically, one direction exhibits C_s symmetry, while the other lacks any symmetry. The resulting spin texture is thus a consequence of anisotropic SOC interactions rather than symmetry protection.

The accidental PST first proposed in the $R3c$ phase of $LiNbO_3$[50] was adopted to construct the Rashba spin-orbit coupling Hamiltonian terms (H_R) up to first order in k, which can be expressed as $H_R = \alpha_1 k_x \sigma_y + k_y(\alpha_2 \sigma_x + \alpha_3 \sigma_z)$ when the electrons are constrained in the k_x-k_y plane. Here, σ_i ($i = x, y, z$) are the Pauli-spin matrices, and the α_i ($i = 1, 2, 3$) are the spin-orbital coupling coefficients with $\alpha_1 = 384$ meV · Å, $\alpha_2 = 120$ meV · Å, and $\alpha_3 = 847$ meV · Å, where the effective $\alpha_R = \sqrt{{\alpha_2}^2 + {\alpha_3}^2}$ represents the spin-splitting strength along the Q-F path about the CBM. The average α_R in the PST region was calculated to be 856 meV · Å, higher than typical 2D Rashba systems with $\alpha_R \approx 1 - 10$ meV · Å, [25,27,28] and corresponding to a Rashba energy of 0.276 eV. Furthermore, a long $\tau_S^{111} \approx 8.9$ ns is obtained when the electrons are constrained in the $(111)_{pc}$ as is the case

for (111)-oriented *R*-$BiInO_3$ films, while a shorter $\tau_S^{001} \approx 555$ ps was calculated when the electrons move along $<100>_{pc}$ as for (001)-oriented *R*-$BiInO_3$ films. The overall parameters for off-stoichiometric *R*-$Bi_{0.75}In_{1.25}O_3$ were similar, with $\alpha_R \approx 883$ meV · Å, $\tau_S^{001} \approx 380$ ps, and $\tau_S^{111} \approx 27$ ns (Note S9 and Figure S15, Supporting Information), which suggests that bismuth deficiency (or indium excess and antisite defects) in *R*-$Bi_{1-x}In_{1+x}O_3$ do not significantly impact the Rashba coefficients or spin-relaxation time.

The primary obstacle in probing the PST, however, is the limitations of experimental techniques (e.g., transient spin–grating spectroscopy[27] and time-resolved magneto-optic Kerr effect[23]), which lack the spatial resolution for sub-micron measurements. Given that the *R*-$Bi_{1-x}In_{1+x}O_3$ films are expected to possess a short spin-orbit scattering length $l_S \approx 0.4$ nm, owing to the high calculated $\alpha_R = 856–883$ meV · Å, alternative approaches to probe this spin texture are necessary. Here, various magneto-transport measurements were conducted, including quantum transport[14,24,25,28,51] and nonreciprocal-charge transport,[7,9,31,52] to explore the Rashba effect and the potential for PST. One challenge to the application of these techniques was the high longitudinal resistivity (ρ_{xx}) of ≈500 Ω · cm of the as-grown *R*-$Bi_{1-x}In_{1+x}O_3$ films (Figure 3d). To enhance the conductivity while preserving the spin texture, electron-carriers were introduced into both (001)- and (111)-oriented *R*-$Bi_{1-x}In_{1+x}O_3$ films by producing oxygen vacancies through annealing under varied oxygen-partial pressures (Figure 3d) (Note S10, Supporting Information and Experimental Section). Formation of oxygen vacancies can make *R*-$Bi_{1-x}In_{1+x}O_3$ films *n* type with increased conductivity as governed by the defect equation $O_o \rightarrow V_O^{\cdot\cdot} + \frac{1}{2}O_2\ (g) + 2e'$. Additionally, X-ray-diffraction studies confirmed that the crystal structure and film thickness remained unchanged after these anneals (Figure S16, Supporting Information). For both (001)- and (111)-oriented *R*-$Bi_{1-x}In_{1+x}O_3$ films annealed at oxygen-partial pressures of 10 mTorr, the ρ_{xx} versus temperature exhibited semiconducting behavior, with ρ_{xx} increasing at lower temperatures (Figure 3e). This can be attributed to the decreased *n* at lower temperatures (Figure 3f) while the mobility (μ) remained nearly constant from 2 to 300 K (Figure 3g). The values of *n* and μ were extracted from the negative slope of the linear transverse resistivity (ρ_{xy}) versus out-of-plane magnetic field (B_{OOP}) curve (Figure S17, Supporting Information). Notably, both (001)- and (111)-oriented *R*-$Bi_{1-x}In_{1+x}O_3$ films exhibited $n < 1.2 \times 10^{18}$ cm^{-3} at $T < 50$ K – one of the conditions for *R*-$Bi_{1-x}In_{1+x}O_3$ to exhibit the bulk-Rashba effect with spin deviation < (5°, 5°). Thus, (001)- and (111)-oriented *R*-$Bi_{1-x}In_{1+x}O_3$ films annealed at oxygen-partial pressures of 10 mTorr, henceforth denoted as annealed (001)- and (111)-oriented *R*-$Bi_{1-x}In_{1+x}O_3$ films, will be used for all the following transport measurements.

2.2.2. Quantum Transport

To elucidate the Rashba effect and potential PST, magneto-transport studies (Experimental Section) were conducted on annealed (001)- and (111)-oriented *R*-$Bi_{1-x}In_{1+x}O_3$ films. Although Rashba-type spin splitting can generally lead to WAL via spin relaxation,[14,53–55] WL can be restored if the spin-relaxation time exceeds the phase decoherence time due to PST, as observed in GaAs quantum wells.[24,25,28] First, annealed (001)-oriented *R*-$Bi_{1-x}In_{1+x}O_3$ films exhibited WAL within the temperature range of 2–10 K (**Figure 4a**), where spin relaxation occurs along the phase-coherent electron path, with a $\tau_S^{001} \approx 66$ ps which is shorter than the phase-decoherence time (τ_φ^{001}) (Figure 4c). The values of τ_φ^{001} and τ_S^{001} were extracted by fitting the magnetoresistance curves to the three-dimensional Fukuyama-Hoshino model[11,56] (Note S11 and Figure S18, Supporting Information). τ_φ^{001} decreases with increasing temperature following a $\approx T^{-0.56}$ trend, such that at 20 K, τ_S^{001} becomes longer than τ_φ^{001}, and crossover from WAL to WL is observed (Figure 4a). Above 50 K, the electron transport devolves into a classical transport regime without phase coherence (Figure 4a). WAL/WL behavior in annealed (001)-oriented *R*-$Bi_{1-x}In_{1+x}O_3$ films could be reproduced for other films with a slightly different chemistry (e.g., $x \approx 0.15$) as long as *n* was maintained below 1.2×10^{18} cm^{-3} (Note S12 and Figure S19, Supporting Information). While WAL in the annealed (001)-oriented *R*-$Bi_{1-x}In_{1+x}O_3$ films corroborates the presence of a Rashba effect in *R*-$Bi_{1-x}In_{1+x}O_3$, it exhibits rapid spin relaxation ($\tau_S^{001} \approx$ 66 ps), faster than what is expected from the DFT calculations ($\tau_S^{001} \approx 380–555$ ps). This could possibly be due to the presence of multiple twinned structural domains since, while unidirectional spin texture is essential for electrons to suppress spin relaxation, backscattered electrons traversing multidomain structures could experience spin textures with varying spin orientations. Moreover, the mosaicity of each domain (Figure S10, Supporting Information) could further deteriorate the unidirectional spin texture. Annealed (111)-oriented *R*-$Bi_{1-x}In_{1+x}O_3$ films, on the other hand, exhibit monodomain structures with high crystallinity and, in turn, demonstrate WL from 2–50 K (Figure 4b), indicating that the spin-orbit timescale is longer than the phase coherence timescale throughout the whole temperature range. It is found that $\tau_S^{111} > 3.36$ ns using the condition for WL ($\tau_\varphi < \tau_S^{111}$) is reasonably consistent with the DFT calculations with $\tau_S \approx 8.9–27$ ns.

Nonetheless, the WL might simply result from the suppression of the Rashba effect, necessitating additional measurements to confirm whether the annealed (111)-oriented *R*-$Bi_{1-x}In_{1+x}O_3$ films retain Rashba-type spin splitting. To investigate this, anisotropic-magnetoresistance and planar-Hall-effect studies (Experimental Section), both of which can arise from spin-momentum locking in topological insulators or Rashba systems,[57,58] were conducted on the annealed (111)-oriented *R*-$Bi_{1-x}In_{1+x}O_3$ films. Both longitudinal (R_{xx}) and transverse resistance (R_{xy}) were measured under an in-plane magnetic field (B_{IP}) of 8 T with a direct current $I^{DC} = 60$ μA at 2 K, while varying the angle (φ) between B_{IP} and I^{DC} (inset, Figure 4d). To eliminate a spurious signal from the Hall effect, antisymmetric terms were removed by using $R_{xx(xy)}^{sym} = \frac{R_{xx(xy)}(I^{DC}=60\ \mu A)+R_{xx(xy)}(I^{DC}=-60\ \mu A)}{2}$ (Figure S20, Supporting Information). The processed R_{xx}^{sym} and R_{xy}^{sym} exhibit a sinusoidal signal with the same amplitude and 45°-phase difference, described by $R_{xx}^{sym} = \frac{(R_\parallel + R_\perp)}{2} + \frac{(R_\parallel - R_\perp)}{2} cos(2\varphi)$ and $R_{xy}^{sym} = \frac{(R_\parallel - R_\perp)}{2} sin(2\varphi)$, where $R_{\parallel(\perp)}$ is the longitudinal resistance when I^{DC} is parallel (perpendicular) to B_{IP} (Figure 4d,e) (Note S13, Supporting Information). Such results, in particular the sinusoidal signals in R_{xx}^{sym} and R_{xy}^{sym} from anisotropic-magnetoresistance and planar-Hall-effect studies, respectively, corroborate the presence of a Rashba effect in the (111)-oriented *R*-$Bi_{1-x}In_{1+x}O_3$ films where Rashba-induced spin-momentum locking can lead

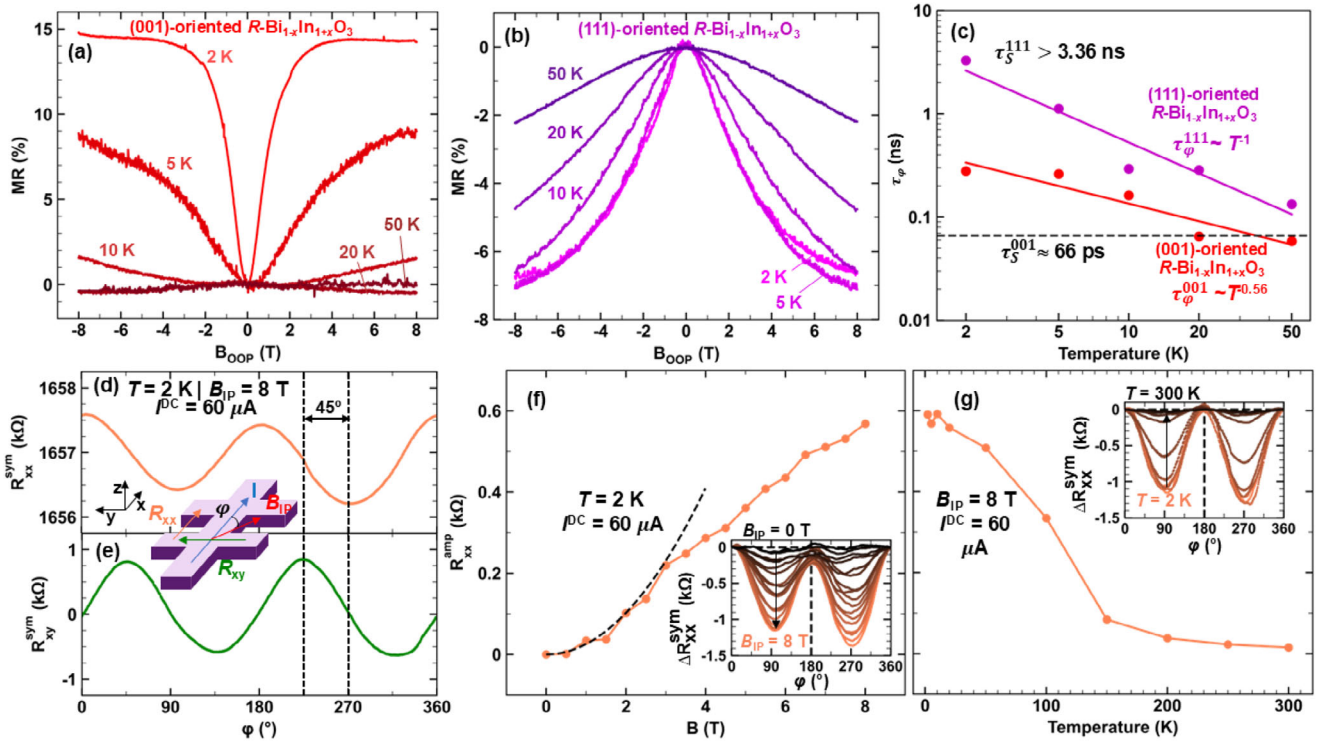

Figure 4. Quantum transport in annealed (001)- and (111)-oriented R-$Bi_{1-x}In_{1+x}O_3$ ($x \approx 0.24$–0.34) films. Magnetoresistance curves in **a)** annealed (001)-oriented and b) annealed (111)-oriented R-$Bi_{1-x}In_{1+x}O_3$ films in the temperature range from 2 to 50 K. c) Phase decoherence time (τ_φ) and spin-relaxation time (τ_{SO}) of the annealed (001)- and (111)-oriented R-$Bi_{1-x}In_{1+x}O_3$ films. d) Longitudinal (R_{xx}^{sym}) and e) transverse resistance (R_{xy}^{sym}) versus φ in annealed (111)-oriented R-$BiInO_3$ films showing anisotropic magnetoresistance (AMR) and planar–Hall effect (PHE), respectively. The inset shows a schematic illustration of the Hall-bar device used to measure AMR and PHE. f) AMR amplitude (R_{xx}^{amp}) measured to the magnetic field (B) at $T = 2$ K. The dashed line is the fitting curve B^2 fitted at the B ranging from 0 to 3 T. The inset shows the measured $\Delta R_{xx}^{sym} = R_{xx}^{sym}(\varphi) - \Delta R_{xx}^{sym}(\varphi = 0°)$ versus φ by varying B from 0 to 8 T. g) PHE amplitude (R_{xy}^{amp}) measured with respect to the temperature (T) at B = 8 T. The inset shows the measured ΔR_{xx}^{sym} versus φ by varying T from 2 to 300 K.

to anisotropic resistance with $R_{||} \neq R_{\perp}$. The amplitudes of the anisotropic magnetoresistance ($R_{xx}^{amp} = \frac{|R_{xx}^{sym}(\varphi=90°) - R_{xx}^{sym}(\varphi=0°)|}{2}$) and planar-Hall effect ($R_{xy}^{amp} = \frac{|R_{xy}^{sym}(\varphi=90°) - R_{xy}^{sym}(\varphi=0°)|}{2}$) show a quadratic dependence with magnetic field $B < 3$ T,[19] while at $B > 3$ T, the signals tend to deviate and saturate (Figure 4f) (Figure S21, Supporting Information). Furthermore, the temperature dependence of the anisotropic magnetoresistance reveals that at higher temperatures (>150 K), thermal energy excites the electrons over the Rashba-induced spin splitting, quenching the anisotropic magnetoresistance (Figure 4g). While coexistence of WL, anisotropic magnetoresistance, and planar-Hall effect qualitatively supports the presence of a bulk-Rashba effect and long spin-relaxation time, further measurements are required to quantify the Rashba strength and compare it with the DFT calculations.

2.2.3. Nonreciprocal-Charge Transport

Nonreciprocal-charge transport, also known as magnetochiral anisotropy, is a non-ohmic nonlinear response to the electric field that can arise from the Rashba effect[7,31,52,59] where the resistance can be expressed as $R(B, I) = R_0(1 + \gamma B \cdot I)$, where B is the external magnetic field, I is the current, and γ is the nonreciprocal coefficient. Using an alternating current $I^{\omega} = I_0 sin(\omega t)$ under a rotating magnetic field $B_{IP} = B_0 cos(\varphi)$, the nonreciprocal signal appears as a second-harmonic resistance $\Delta R_{xx}^{2\omega} = \frac{1}{2}\Delta\gamma R_0 B_0 I_0 cos(\varphi) sin(2\omega t - \pi/2)$, where the amplitude linearly depends on B_0 and I_0 (Experimental Section). Using the same Hall-bar devices used above for the annealed (111)-oriented R-$Bi_{1-x}In_{1+x}O_3$ films (inset, Figure 4e), it was found that $\Delta R_{xx}^{2\omega}$ exhibited sinusoidal response ($\Delta R_{xx}^{2\omega} \approx R_{amp}^{2\omega} \sin(\varphi)$) (**Figure 5a**) with fixed $B_0 = 8$ T and varied current $I_0 = 10$–60 μA. $R_{amp}^{2\omega}$ linearly scaled with I_0 as expected from $R_{amp}^{2\omega}/R_0 = \frac{1}{2}\gamma B_0 I_0$, from which γ can be extracted as ≈0.33 $A^{-1}T^{-1}$ (Figure 5b). Next, B_0 was varied from -8 to 8 T and a fixed $I_0 = 60$ μA, again $R^{2\omega}$ exhibits a sinusoidal response (Figure 5c). The sign of $R_{amp}^{2\omega}$ was reversed upon reversing the sign of B_0, and similarly, confirmed the γ value as ≈0.33 $A^{-1}T^{-1}$ (Figure 5d). Although a thermoelectric effect due to a thermal gradient ∇T can also give a spurious signal with the same angular dependence as nonreciprocal charge transport,[60] its contribution was negligible, as revealed by small $\Delta R_{xy}^{2\omega}$ compared to $\Delta R_{xx}^{2\omega}$ (Note S14 and Figure S22, Supporting Information).

Furthermore, as nonreciprocal charge transport is directly coupled to the Rashba effect, α_R can be determined from the nonreciprocal coefficient γ. Using a semiclassical Boltzmann theory in a three-dimensional Rashba system[7] (Note S15, Supporting

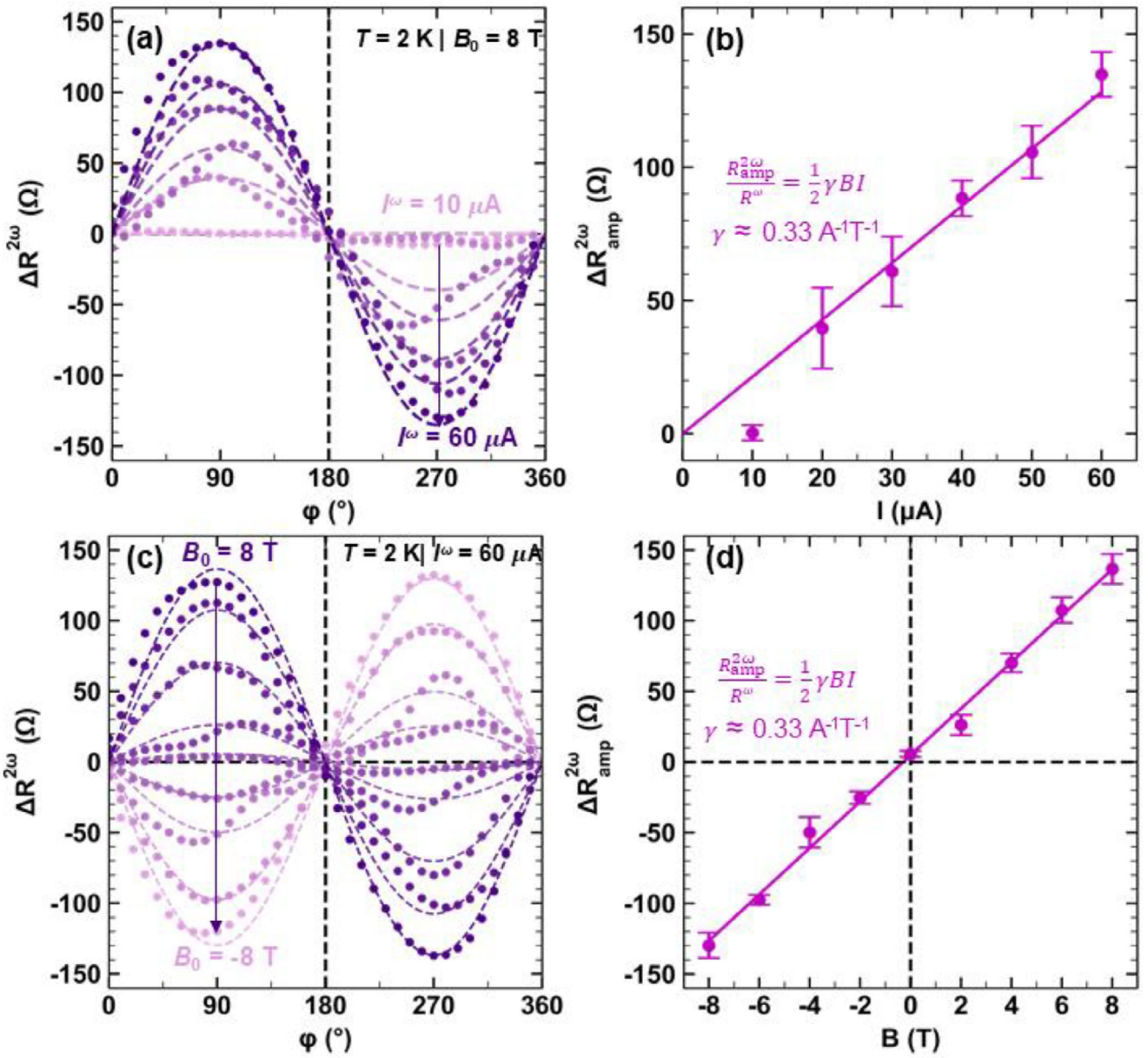

Figure 5. Nonreciprocal charge transport in annealed (111)-oriented R-$Bi_{1-x}In_{1+x}O_3$ ($x \approx 0.24$–0.34) films. a) Second-harmonic resistance ($\Delta R_{xx}^{2\omega}$) versus φ as a function of the AC (I^{ω}) varying from 10 to 60 μA. b) Extracted $\Delta R_{amp}^{2\omega}$ with respect to I^{ω}. c) $\Delta R_{xx}^{2\omega}$ versus φ as a function of the magnetic field (B) from 8 to −8 T. d) Extracted $\Delta R_{amp}^{2\omega}$ with respect to B. Dashed lines in (a) and (c) are the fitting curves $\Delta R_{amp}^{2\omega}\sin(\varphi)$. Solid lines in (b) and (d) are the fitting lines $\Delta R_{amp}^{2\omega}/R^{\omega} \sim \frac{1}{2}\gamma BI$ where $\gamma \approx 0.33\ A^{-1}T^{-1}$.

Information), $\alpha_R = (\frac{3\pi}{A(m^*)^2 E_F^2 \gamma})^{\frac{1}{2}} \approx 760$ meV · ∀, which is comparable to $\alpha_R \approx 856$ meV · Å obtained from our DFT calculations. Although α_R can also be extracted from WAL in the annealed (001)-oriented R-$Bi_{1-x}In_{1+x}O_3$ films as $\alpha_R = \sqrt{e\hbar^3 B_{so}}/m^* \approx 147$ meV · ∀, α_R is underestimated from this method. The discrepancy arises from the assumption in the WAL model that every momentum-dependent-scattering event leads to spin relaxation, with the degree of relaxation governed by the Rashba strength. Spin relaxation in (001)-oriented R-$Bi_{1-x}In_{1+x}O_3$ films, however, likely occurs across domain walls, while the momentum-dependent scattering within a domain should not lead to spin relaxation. If all momentum-dependent scatterings lead to spin relaxation in the R-$Bi_{1-x}In_{1+x}O_3$ films with $\alpha_R \approx 760$ meV · Å, then $l_S \approx 0.55$ nm and $\tau_S \approx 2.5$ ps should be obtained; values which are at least two orders of magnitude lower than l_S^{111} (> 20 nm) and τ_S^{111} (> 3.36 ns). These results all indicate that annealed (111)-oriented R-$Bi_{1-x}In_{1+x}O_3$ films exhibit long $\tau_S >$ 3.36 ns even with a high $\alpha_R \approx 760$ meV · Å, whereas typical Rashba systems suffer from spin relaxation induced by

Table 1. R1. Rashba parameter and spin relaxation time in multiple Rashba systems.

	R-$Bi_{1-x}In_{1+x}O_3$ (This Work)	GaAs Quantum Well[9,12]	GaSe[13]	InSe [14,61]	$LaAlO_3/SrTiO_3$ [15,16]
α_R [meV · Å]	≈760	≈5	≈100	≈2	≈2–50
τ_S [ps]	≈3.36	≈10–300	≈0.01–0.1	≈1–7	≈0.1

the Rashba effect (**Table 1**). All told, the observed weak localization, anisotropic magnetoresistance, planar Hall effect, and nonreciprocal-charge transport are all consistent with the existence of unidirectional spin texture; however, further study will be required to directly map this spin texture.

3. Conclusion

In summary, a new polar $LiNbO_3$-type $Bi_{1-x}In_{1+x}O_3$ phase with $x \approx 0.15$-0.34 was stabilized, which exhibits a bulk-Rashba effect with a long τ_S. Through epitaxial thin-film growth, the metastable polar R-$Bi_{1-x}In_{1+x}O_3$ phase was stabilized and found to exhibit higher electrical conductivity, reduced optical bandgap, and enhanced dielectric and piezoelectric responses as compared to previously discovered non-polar O-$Bi_{1-x}In_{1+x}O_3$. Combining first-principles calculations and multimodal transport measurements, compelling evidence was provided to show that R-$Bi_{1-x}In_{1+x}O_3$ exhibits a bulk-Rashba effect with suppressed spin relaxation enabled by a unidirectional spin texture. Specifically, (111)-oriented R-$Bi_{1-x}In_{1+x}O_3$ films with monodomain structure exhibited weak localization – a signature of the enhanced $\tau_S > 3.36$ ns. Additional transport studies on the (111)-oriented R-$Bi_{1-x}In_{1+x}O_3$ films, including anisotropic magnetoresistance, planar-Hall effect, and nonreciprocal charge transport, further corroborated the presence of the bulk-Rashba effect with $\alpha_R \approx 760$ meV · Å. The realization of the bulk-Rashba effect alongside long τ_S in polar R-$Bi_{1-x}In_{1+x}O_3$ offers new opportunities to understand and harness spin-orbit coupling phenomena for robust spintronic applications.

4. Experimental Section

Thin-Film Growth: $Bi_{1-x}In_{1+x}O_3$ thin films (100 nm-thick) were grown using pulsed-laser deposition with a KrF laser (LPX 305; Coherent) with a wavelength of 248 nm. First, to explore the possible structural phases of $Bi_{1-x}In_{1+x}O_3$, an excess-bismuth ceramic target with the composition $Bi_{1.1}InO_3$ was used to grow $Bi_{1-x}In_{1+x}O_3$ films on MgO (001), $DyScO_3$ $(110)_O$, and $SrTiO_3$ (111) substrates at growth temperatures T_g = 550–650 °C. To investigate whether bismuth loss at higher T_g can be compensated for, an additional ceramic target with further bismuth excess and composition $Bi_{1.3}InO_3$ was used to grow $Bi_{1-x}In_{1+x}O_3$ films on $DyScO_3$ $(110)_O$ substrates at T_g = 650, 675, 700, and 725 °C. Additionally, $Bi_{1-x}In_{1+x}O_3$ films were also grown on other substrates, namely, $NdScO_3$ $(110)_O$, $GdScO_3$ $(110)_O$, $SrTiO_3$ (001), $SrTiO_3$ (110), $(LaAlO_3)_{0.3}(Sr_2TaAlO_6)_{0.7}$ (LSAT) (001), and $LaAlO_3$ (001) at T_g = 650 °C to examine substrate effects on phase stabilization. For all the $Bi_{1-x}In_{1+x}O_3$ growths, a dynamic oxygen partial pressure of 100 mTorr, laser fluence of 1.0 J cm^{-2}, laser repetition frequency of 20 Hz, and an on-axis target-to-substrate distance of 57 mm were employed. For out-of-plane dielectric and piezoelectric measurements, 30 nm $La_{0.67}Sr_{0.33}MnO_3$ / 100 nm $Bi_{1-x}In_{1+x}O_3$ / 30 nm $La_{0.67}Sr_{0.33}MnO_3$ heterostructures were grown on $SrTiO_3$ (110), $SrTiO_3$ (111), and $DyScO_3$ $(110)_O$ substrates. Before and after the deposition of the $Bi_{1-x}In_{1+x}O_3$ layer, the $La_{0.67}Sr_{0.33}MnO_3$ layers were grown at T_g = 650 °C in a dynamic oxygen partial pressure of 100 mTorr, laser fluence of 1.0 J cm^{-2}, laser repetition frequency of 2 Hz, and an on-axis target-to-substrate distance of 57 mm. For all the growths, the films were cooled down from the growth temperature to room temperature at a rate of 10 °C min^{-1} in a static oxygen partial pressure of ≈700 Torr.

Structural Characterization using X-Ray Diffraction: The crystal structure of each film was studied using symmetric θ–2θ linescans, reciprocal space mapping (RSM), and X-ray reflection (XRR). A high-resolution X-ray diffractometer (X'Pert 3 MRD; Panalytical,) with copper Kα radiation (1.540598 Å), and a detector (PIXcel3D-Medipix3) were utilized. Fixed divergence slit of 1/2°, 1/16°, and 1/32° were used for linescans, RSM, and XRR, respectively. Bragg–Brentano θ–2θ geometry was used to characterize the crystal structure perpendicular to the substrate plane, and X-ray rocking curves about the R-$Bi_{1-x}In_{1+x}O_3$ 111_{pc}- and 002_{pc}- diffraction conditions were measured to assess the crystalline quality of the films. RSMs were studied about 002_{pc}- and 103_{pc}- diffraction conditions for (001)-oriented R-$Bi_{1-x}In_{1+x}O_3$ films grown on $DyScO_3$ $(110)_O$ and 111_{pc}- and 330_{pc}- diffraction conditions for (111)-oriented R-$Bi_{1-x}In_{1+x}O_3$ films grown on $SrTiO_3$ (111). XRR was used to determine the thickness of R-$Bi_{1-x}In_{1+x}O_3$ films in their as-grown state and after annealing.

Time-of-Flight Secondary Ion Mass Spectroscopy: High mass resolution depth profiles were performed using a time-of-flight secondary ion mass spectroscopy (TOF-SIMS) NCS instrument, which combines a TOF.SIMS 5 instrument (ION-TOF GmbH, Münster, Germany) and an in situ scanning probe microscope (NanoScan, Switzerland) within the Shared Equipment Authority at Rice University. The analysis field of view was 150 × 150 μm^2 (Bi_3^+ at 30 keV, 0.3 pA) with a raster of 128 × 128 along the depth profile. Charge compensation with an electron flood gun has been applied during the analysis. An adjustment of the charge effects has been performed using a surface potential. The cycle time was fixed to 100 μs (corresponding to m/z = 0–911 a.m.u mass range). The sputtering raster was 500 × 500 μm^2 (Cs^+ at 2 keV, 105 nA). The beams were operated in non-interlaced mode, alternating one analysis cycle and one per frame of sputtering, followed by a pause of three seconds for the charge compensation.

The MCs_n^+ (n = 1, 2) depth profiling was also used to improve the understanding of the data. This is a useful method, mainly applied to quantify alloys but also to identify any ionic compounds. The cesium primary beam is used for sputtering during the depth profile and permits to detect MCs^+ or MCs_2^+ cluster ions, where M is the element of interest combined with one or two cesium atoms. The advantages of following MCs^+ and MCs_2^+ ions during ToF-SIMS analysis include the reduction of matrix effects and the possibility of detecting compounds from both electronegative and electropositive elements and compounds.

All depth profiles were point-to-point normalized by the total-ion intensity, and the data were plotted using a 10-point adjacent averaging. Both normalization and smoothing permitted a better comparison of the data from the different samples. The depth calibrations were established using the interface tool in *SurfaceLab* version 7.3 software from ION-TOF GmbH to identify the different interfaces and based on the measured crater thicknesses using in situ SPM in linescan mode. The sensitivity of each element was calibrated using the $Bi_{1.1}InO_3$ target as a reference sample.

UV-Vis Spectroscopy: Transmission geometry ultraviolet–visible-light (UV–vis) spectroscopy was employed (U-3000 UV/Vis spectrophotometer; Hitachi). To account for the contribution from the substrates, transmission studies of O- and R-$Bi_{1-x}In_{1+x}O_3$ films were measured simultaneously with bare substrates of the same type, and relative transmission from

the film with respect to the bare substrate (T) was obtained. To minimize the absorption from the substrate, measurements were taken from (001)-oriented R-$Bi_{1-x}In_{1+x}O_3$ films grown on $GdScO_3$ $(110)_O$ substrates and O-$Bi_{1-x}In_{1+x}O_3$ films grown on MgO (001) substrates. Substrates used as a reference, MgO (001) and $GdScO_3$ $(110)_O$, were annealed under the same conditions as the $Bi_{1-x}In_{1+x}O_3$ growth condition: heater temperature of 650 °C in a dynamic oxygen partial pressure of 100 mTorr. The absorption coefficient (α) was calculated from T using $\alpha = -2.303 \cdot log(T)/t$, where $t = 100$ nm is the film thickness. The direct optical bandgap (E_g) was obtained using the relation $(\alpha h\upsilon)^2 = B(h\upsilon - E_g)$, where h is Planck's constant, B is a linear constant, and υ is the photon energy.

Electrical, Dielectric, and Piezoelectric Characterization: For in-plane measurements, platinum interdigitated electrodes (IDEs) were sputtered on top of (001)-oriented R-$Bi_{1-x}In_{1+x}O_3$ films grown on $DyScO_3$ $(110)_O$, (111)-oriented R-$Bi_{1-x}In_{1+x}O_3$ films grown on $SrTiO_3$ (111), and (100)-oriented O-$Bi_{1-x}In_{1+x}O_3$ films grown on MgO (001) with 2 µm finger spacings and 100 µm arm lengths. The IDE structures were patterned by photolithography via a maskless aligner (MLA 150; Heidelberg) using AZ MiR 701 Photoresist. After patterning, 50 nm of platinum was deposited using DC sputtering. After reaching the base pressure of $\approx 1 \cdot 10^{-7}$ Torr, the chamber was purged with argon, and platinum was deposited at room temperature in a dynamic argon partial pressure of 7 mTorr and target power of 15 W with a growth rate of 8 nm min^{-1}. For out-of-plane dielectric and piezoelectric measurements, out-of-plane geometry circular capacitors were fabricated on the following $Bi_{1-x}In_{1+x}O_3$ heterostructures: 30 nm $La_{0.67}Sr_{0.33}MnO_3$ / 100 nm R-$Bi_{1-x}In_{1+x}O_3$ / 30 nm $La_{0.67}Sr_{0.33}MnO_3$ / $DyScO_3$ $(110)_O$, 30 nm $La_{0.67}Sr_{0.33}MnO_3$ / 100 nm R-$Bi_{1-x}In_{1+x}O_3$ / 30 nm $La_{0.67}Sr_{0.33}MnO_3$ / $SrTiO_3$ (111), and 30 nm $La_{0.67}Sr_{0.33}MnO_3$ / 30 nm thick O-$Bi_{1-x}In_{1+x}O_3$ / 30 nm $La_{0.67}Sr_{0.33}MnO_3$ / $SrTiO_3$ (110). Circular capacitors 25 µm in diameter were fabricated using $La_{0.67}Sr_{0.33}MnO_3$ as the top electrode via photolithography followed by argon-ion milling (Nanoquest; Intlvac). After reaching the base pressure below $5 \cdot 10^{-6}$ Torr, the chamber was filled with argon with a dynamic argon partial pressure of $2.25 \cdot 10^{-4}$ Torr. The stage temperature was then set to 15 °C, and a ≈40 nm layer was ion milled with the etch rate of ≈25 nm min^{-1} using a beam voltage of 500 V, a beam current of 38 mA, and accelerator voltage of 100 V while the stage was rotating with the speed of 10 rpm.

The leakage current density as a function of DC electric field up to ±167 kV cm^{-1} with a soak time of 100 ms was measured using a ferroelectric tester (Precision Multiferroic Tester; Radiant Technologies, Inc.) at room temperature. The polarization response was measured as a function of electric field with the field strength up to ±1.2 MV cm^{-1} and fixed frequency of 10 kHz using the same tester. For polarization measurements at low temperature (≈80 K), a cryogenic probe station (TTPX; Lake Shore Cryotronics) was used. Dielectric constant and loss tangent as a function of AC electric field frequency were measured using an impedance analyzer (E4990A; Keysight Technologies) with a fixed AC field strength of 1 kV cm^{-1} and frequency ranging from 1 kHz to 1 MHz. Dielectric constant $\epsilon_r = tC_p/A\epsilon_0$ was calculated, where $t = 100$ nm is the film thickness, C_p is the parallel capacitance measured using an impedance analyzer, A is the capacitor area of $4.91 \cdot 10^{-6}$ cm^2, and ϵ_0 is the permittivity of vacuum ($8.854 \cdot 10^{-14}$ F cm^{-1}). The electromechanical response was measured using laser Doppler vibrometry (Polytec GmbH).[49] The vertical surface displacement was measured using 2 µm-diameter HeNe laser beam ($\lambda = 633$ nm) incident on top of the circular capacitor while the electrical field was simultaneously stimulated by a ferroelectric tester with a fixed frequency of 1 kHz and electric field strength up to ±200 kV cm^{-1}.

E_{hull} Calculations: Density-functional theory (DFT) calculations were performed with the Vienna ab initio Simulation Package (VASP).[62–65] The projector augmented wave (PAW) pseudopotentials explicitly included 15 valence electrons ($6s^2$, $5d^{10}$, $6p^3$) for bismuth, 13 valence electrons ($5s^2$, $4d^{10}$, $5p^1$) for indium, and six valence electrons ($2s^2$, $2p^4$) for oxygen. Spin-orbit coupling was included for all calculations. All crystal structures were fully relaxed until ionic forces were less than 10^{-2} eV $Å^{-1}$. The electronic convergence threshold was set to 10^{-6} eV, and the plane-wave energy cutoff (650 eV) and k-point sampling densities (ranging from 180 points per $Å^{-3}$ for pristine $BiInO_3$ to 1400 points per $Å^{-3}$ for metallic bismuth) were selected such that total energies were converged to within 1 meV per atom. For insulating systems, k-point integration was performed with the tetrahedron method. Methfessel–Paxton smearing was used for metals, where the smearing width of 25 meV was chosen such that the entropic contribution was less than 10^{-4} eV per atom. To assess sensitivity to the choice of exchange-correlation functional, most calculations were repeated for multiple functionals, including LDA,[66–68] PBE,[69] PBEsol,[70] r2SCAN,[71,72] and SCAN.[73,74] Results referenced in the text were computed with PBEsol unless otherwise stated. Computed energies above the hull for all five functional choices are shown (Figure 1f and Figure S6, Supporting Information).

The convex hull of the Bi–In–O system was computed from Materials Project data;[75] the relevant stable phases of Bi, In, O_2, Bi_2O_3, and In_2O_3 were recalculated using the parameters described above. Off-stoichiometric structures in the $Bi_{1-x}In_{1+x}O_3$ system were obtained by constructing supercells and selecting bismuth sites for indium substitution. In the conventional supercell, two different substitutional defect configurations are presented within the 33%–67% substitution range: one in which substitutional sites are clustered nearby within the cell, and one in which they are dispersed throughout the cell. In the larger $2 \times 2 \times 2$ supercell, five randomly-selected configurations are presented for each substitution fraction. The polarization of the $R3c$ phase was computed using the Berry-phase approach with the interpolation scheme implemented in pymatgen,[76] using the previously described calculation parameters and the PBEsol exchange-correlation functional. The nonpolar R-$3c$ reference phase was generated using the PSEUDO tool[77] of the Bilbao Crystallographic Server, as described in Ricci et al.[78] .

Electronic-Band-Structure Calculations: Total energy calculations were based on DFT within the generalized gradient approximation (GGA) utilizing the revised Perdew-Becke-Erzenhof functional for solids (PBEsol)[70] implemented in the VASP.[63–65] A 500 eV plane wave cutoff energy was used for all calculations and the PAW method[79] with 15 valence electrons ($6s^2$, $5d^{10}$, $6p^3$) for bismuth, 13 valence electrons ($5s^2$, $4d^{10}$, $5p^1$) for indium, and six valence electrons ($2s^2$, $2p^4$) for oxygen. Gaussian smearing (0.10 eV width) was utilized for the Brillouin-zone integrations. The k-point sampling is tested to be sufficient for different cell sizes. The convergence thresholds for the electronic relaxation and atomic-structure relaxation are 10^{-6} eV and 0.01 eV $Å^{-1}$, respectively. Spin-orbit coupling (SOC) effects were not considered in the structure relaxation, but were included in the band-structure calculations for the spin textures.

$k \cdot p$ Model: Following established methods,[50] the $k \cdot p$ model was constructed using the following theory and protocol. When including the spin ($|S| = 1/2$) in the wavefunction, there is a spin-orbital coupling (SOC) term $\propto s \cdot l$ where s and l are spin and orbital angular momenta, respectively, in $\mathcal{H}$. $\mathcal{H}(\Delta k)$ becomes: $\mathcal{H}(\Delta k) = \mathcal{H} + \frac{\hbar \Delta k}{m} \cdot (p + \frac{\hbar}{4mc^2}\sigma \times \nabla V) + \frac{\hbar^2}{2m}(\Delta k)^2$ as described in References[80,81] . $\mathcal{H}(\Delta k)$ can be solved using a group-theory analysis with the following steps. Here, $\mathcal{H}(\Delta k)$, as an example is solved, and set $k_0 = 0$:

1) Choosing a basis set of wavefunctions, for example, $D^{\frac{3}{2}}$ can be used in a four-band $k \cdot p$ model.
2) Decomposing $D^{\frac{3}{2}}$ into a sum of irreducible representations (*irreps*) (e.g., $\mathcal{R}$) using the character table of a double group at k_0.

After accomplishing (1) and (2), the irreducible symmetric matrix is obtained by considering

1) $\mathcal{H}^{\alpha,\beta}_{i,j}(k) = \sum_{\gamma,l}(\psi^{\alpha}_i, \mathcal{H}^{\bar{\gamma}}_l \psi^{\beta}_j) = \sum_{\gamma,l}(^{\alpha}_{i}\tau|^{\bar{\gamma}\,\beta}_{l\;\;j}) \| \mathcal{H}^{\bar{\gamma}}_l(k) \|$, where $\mathcal{H}^{\alpha,\beta}_{i,j}(k)$ comprises the matrix of the $k \cdot p$ model, and k is a small wavevector away from k_0, ψ^{α}_i and ψ^{β}_j are $D^{\frac{3}{2}}$ wavefunctions, $\mathcal{H}^{\bar{\gamma}}_l$ is the Taylor expansion of k, where $\bar{\gamma}$ and l indicate the conjugate *irreps* of the summations over the *irreps* obtained by decomposing $\mathcal{R} \times \mathcal{R}$ and the dimension of $\mathcal{H}^{\bar{\gamma}}$, respectively. $(^{\alpha}_{i}\tau|^{\bar{\gamma}\,\beta}_{l\;\;j})$ are the Clebsch–Gordon (C-G) coefficients and $\| \mathcal{H}^{\bar{\gamma}}_l(k) \|$ is the irreducible symmetric tensors of k that can be obtained by using the projection operator technique.

2) Last, the final Hamiltonian is obtained as $\mathcal{H} = \sum_{\gamma,l} X_l^{\bar{\gamma}} ||H_l^{\bar{\gamma}}(k)||$, where $X_l^{\bar{\gamma}} = (^{\alpha}_{i}\tau|^{\bar{\gamma}\beta}_{l\,j})$ is the irreducible symmetric matrix.

In this study, k_x lies in a x–z mirror plane, and k_y is perpendicular to the x–z mirror plane. Thus, k_x has A_1 symmetry of the C_s double point group (A is an irreducible representation), and k_y has A_2 symmetry. A basis set of wavefunctions having a symmetry of $D^{1/2}$ was adopted, which are two-dimensional, and the two components have $\bar{E}^2$ and $\bar{E}^1$ symmetries, respectively. With this information, a Hamiltonian with C_s symmetry was built, where the SOC terms were constrained in the $k_x - k_y$ plane were considered up to the first order in k, and can be expressed as:

$$\mathcal{H} = \gamma_1 k_x \sigma_y + k_y (\gamma_2 \sigma_x + \gamma_3 \sigma_z) \tag{1}$$

or alternatively in matrix form as:

$$\mathcal{H} = \mathcal{H}_0 + \begin{vmatrix} \mathcal{H}'_{11} & \mathcal{H}'_{12} \\ \mathcal{H}'_{12*} & -\mathcal{H}'_{11} \end{vmatrix} \tag{2}$$

where, $\mathcal{H}'_{11} = \gamma_1 k_x$, $\mathcal{H}'_{12} = -\gamma_2 k_y i + \gamma_3 k_y$, $\mathcal{H}'^{*}_{i2}$ is the conjugate part of $\mathcal{H}'_{i2}$, and γ is a real constant. The basis set of the wavefunctions for the two-band model was chosen as $D^{1/2}$, which represents the wavefunctions comprised of p orbitals of spin 1/2 of bismuth. σ_y along the z direction in the spin coordinate was adopted, and Cartesian coordinates in the trigonal cell were specified as $[1\bar{1}0]$ for y and [111] as for z were used. The resulting energy is then:

$$E = \begin{cases} E_0 - \sqrt{(\gamma_1 k_x)^2 + (\gamma_2 k_y)^2 + (\gamma_3 k_y)^2} \\ E_0 + \sqrt{(\gamma_1 k_x)^2 + (\gamma_2 k_y)^2 + (\gamma_3 k_y)^2} \end{cases} \tag{3}$$

where at $k_x = 0$ the Rashba coefficient can be defined as $\sqrt{{\gamma_2}^2 + {\gamma_3}^2}$ along the k_y of Q–F path. Although the R-$Bi_{1-x}In_{1+x}O_3$ phase is relaxed in the films, the epitaxial strain may still affect the SOC coefficients, effective electron mass, and the spin-relaxation time. The band structure of the $R3c$ structure under 0% epitaxial strain (i.e., $a = b$) was further calculated, where $\alpha_1 = 370$ meV · Å, $\alpha_2 = 81$ meV · Å and $\alpha_3 = 840$ meV · Å were obtained. The Rashba coefficient is 844 meV · Å, and the spin-relaxation time is 9.9 ns.

Spin-Relaxation Time Calculations: Based on previous work,[50] a spin-relaxation time can be obtained by solving a spin-charge density dynamic equation expressed as:

$$\partial_t \hat{g} + \nabla_R \cdot \left\{ \frac{1}{2} \overline{\hat{V}}, \hat{g} \right\} + i \left[\overline{B(k)} \cdot \hat{\sigma}, \hat{g} \right] + \frac{\hat{g}}{\tau} = \frac{\hat{\rho}(R,T)}{\tau} \tag{4}$$

where $\hat{V} = \partial \mathcal{H} / \partial k$ and $B(k) = (\gamma_1 k_y, \gamma_2 k_x, \gamma_3 k_x)$, $\overline{\hat{V}}$ and $\bar{B}$ indicates the average quantities; τ is the momentum scattering time; $\hat{g}$ and $\hat{\rho}$ are thermal average distribution function and density matrix, respectively, which can be written as:

$$\hat{\rho} = \rho_c \sigma_0 + \rho_x \sigma_x + \rho_y \sigma_y + \rho_z \sigma_z \tag{5}$$

$$\hat{g} = g_c \sigma_0 + g_x \sigma_x + g_y \sigma_y + g_z \sigma_z \tag{6}$$

With the model derived above, here is the spin-diffusion coefficient:

$$D = \int \frac{d\theta}{2\pi} \begin{bmatrix} 1 - i\omega\tau + iq \cdot \nu\tau & i\gamma_2 q_y \tau & i\gamma_1 q_x \tau & i\gamma_3 q_y \tau \\ i\gamma_2 q_y \tau & 1 - i\omega\tau + iq \cdot \nu\tau & 2\gamma_3 \overline{k_y} \tau & -2\gamma_1 \overline{k_x} \tau \\ i\gamma_1 q_x \tau & -2\gamma_3 \overline{k_y} \tau & 1 - i\omega\tau + iq \cdot \nu\tau & 2\gamma_2 \overline{k_y} \tau \\ i\gamma_3 q_y \tau & 2\gamma_1 \overline{k_x} \tau & -2\gamma_2 \overline{k_y} \tau & 1 - i\omega\tau + iq \cdot \nu\tau \end{bmatrix}^{-1} \tag{7}$$

where $\bar{k}$ is the thermal average momentum, and there is a constant of $\hbar$ in $\bar{k}$ for the simplicity of writing the equation. Then, the enhanced spin-relaxation time frequency $i\omega$ is numerically computed when the determinant of $D - I$ is zero where I is the unit matrix.

Electrical-Transport Measurements: R-$Bi_{1-x}In_{1+x}O_3$ films were annealed in a reducing environment with low oxygen partial pressure to control the oxygen-vacancy concentration and the electron-carrier density. To complete the anneals, the films were mounted in a pulsed-laser deposition chamber and annealed at the heater temperature of 300 °C, and dynamic oxygen-partial pressure from 1–1000 mTorr. First, the chamber was pumped to a pressure $<1{\cdot}10^{-5}$ Torr, followed by purging with oxygen until the pressure was ≈1 Torr, before then pumping again to a pressure $<1{\cdot}10^{-5}$ Torr. Once the chamber reaches the base pressure ($<1{\cdot}10^{-5}$ Torr), oxygen-partial pressure was set at the targeted annealing pressure and the substrate was heated at the rate of 20 °C min^{-1} followed by the annealing time of 30 min at the heater temperature of 300 °C, and then cooled down to room temperature at the rate of 10 °C min^{-1}. Once the heater temperature is below 80 °C, the chamber was then vented to the atmosphere and removed.

For electrical transport measurements, Hall-bar devices were fabricated on the annealed (001)- and (111)-oriented R-$Bi_{1-x}In_{1+x}O_3$ films via a two-step-photolithography process. First, the films were spin–coated with photoresist (MiR 701), and the six-point contact Hall-bar geometry was patterned by photolithography using a maskless aligner (MLA 150; Heidelberg instruments) with the channel length $l \approx 10$ µm and channel width $w \approx 10$ µm. The films were argon-ion milled (Nanoquest; Intlvac) to a depth of ≈120 nm to fully remove the unwanted film layer (100 nm in thickness). After reaching the base pressure ($<5 \times 10{-}^6$ Torr), the chamber pressure was adjusted to a dynamic argon partial pressure of 2.25×10^{-4} Torr. The stage temperature was then set to 15 °C and the film was ion milled with the etch rate of ≈25 nm min^{-1} using a beam voltage of 500 V, beam current of 38 mA, and accelerator voltage of 100 V while the stage was rotating a the speed of 10 rpm. After ion milling, the remaining photoresist was washed away using acetone. The second photolithography process was conducted to define the contact electrodes with dimensions 100 × 100 µm. Platinum was then deposited to a thickness of 150 nm as a contact electrode using DC sputtering. After reaching the base pressure of ≈1×10^{-7} Torr, the chamber was purged with argon, and platinum was deposited at room temperature in a dynamic argon partial pressure of 7 mTorr and target power of 15 W with a growth rate of 8 nm min^{-1}.

Magneto-transport measurements were conducted on the Hall-bar devices fabricated on the annealed (001)- and (111)-oriented R-$Bi_{1-x}In_{1+x}O_3$ films using the physical properties measurement system (Cryogenic Limited). For resistivity (ρ_{xx}) measurements, a DC source (Keithley 2400) was used with a fixed direct currrent (I^{DC}) of 1 µA and the longitudinal voltage (V_{xx}) was measured using a nanovoltmeter (Keithley 2182A). While measuring V_{xx}, the stage temperature was cooled down from 300 to 10 K at the rate of 2 K min^{-1} and from 10 to 2 K at the rate of 0.2 K min^{-1}.

For Hall-measurements, a fixed $I^{DC} = 1$ µA was sourced using a DC source (Keithley 2400) and the transverse voltage (V_{xy}) was measured using a nanovoltmeter (Keithley 2182A) at fixed temperatures of 2, 5, 10, 20, 50, 100, 200, and 300 K. After reaching each target temperature, the stage was left idle for an hour to allow for the stage temperature to stabilize. The static out-of-plane magnetic field (B_{OOP}) was swept from −8 to 8 T (forward-sweep) and then back to −8 T (backward-sweep) at a ramping rate of 0.2 T min^{-1}. The R_{xy} values from the forward-sweep and the backward-sweep were averaged to eliminate the drift in the signal.

Magnetotransport measurements probing weak (anti)loczlization were conducted using a DC source (Keithley 2400) with a fixed direct current of $I^{DC} = 1$ µA and the V_{xx} was measured using a nanovoltmeter (Keithley 2182A) at fixed temperatures of 2, 5, 10, 20, and 50 K. After reaching each target temperature, the stage was left idle for an hour to allow for the stage temperature to stabilize. Similar to Hall-measurements, B_{OOP} was swept from −8 to 8 T (forward-sweep) and then back to −8 T (backward-sweep) at a ramping rate of 0.2 T min^{-1}. The R_{xx} values from the forward-sweep and the backward-sweep were averaged to eliminate the drift in the signal.

Anisotropic magnetoresistance (AMR) and planar-Hall-effect (PHE) measurements were conducted by measuring V_{xx} (for AMR) and

V_{xy} (for PHE) under a static in-plane magnetic field (B_{IP}). A fixed direct current of I^{DC} = 60 μA was sourced using a DC source (Keithley 2400), while V_{xx} and V_{xy} were measured using a nanovoltmeter (Keithley 2182A) at fixed temperatures of 2, 5, 10, 20, 50, 100, 200, and 300 K. After reaching each target temperature, the stage was left idle for an hour to allow for the stage temperature to stabilize. B_{IP} was set to 0, ±0.5, ±1, ±2, ±3, ±4, ±5, ±6, ±7, and ±8 T and the sample was rotated from 0° to 360° at a rotating speed of 20° min^{-1}.

For nonreciprocal charge transport, the second harmonic signal ($R_{xx}^{2\omega} = V_{xx}^{2\omega}/I^{\omega}$) was measured under a rotating B_{IP} at a fixed stage temperature of 2 K. Sinusoidal alternating current (I^{ω}) with an amplitude of 10–60 μA and a frequency of 1.7 Hz was sourced using an AC source (Keithley 6221), and the longitudinal second harmonic voltage ($V_{xx}^{2\omega}$) was measured using a lock-in amplifier (Stanford Research Systems SR830). The quadrature component *Y*, with a 90° phase shift from the signal, was sampled as $V_{xx}^{2\omega}$ with a sensitivity of 10 mV, time constant of 10 s with 18 db oct^{-1} rolloff. An external reference signal was generated from Keithley 6621. B_{IP} was fixed at 0, ±2, ±4, ±6, ±8 T where the sample rotated with 10° step size. $V_{xx}^{2\omega}$ was measured after a stabilization period of 180 s for each step.

Supporting Information

Supporting Information is available from the Wiley Online Library or from the author.

Acknowledgements

D.K. acknowledges the support of the National Science Foundation under Grant DMR-2102895. X.-Z.L. acknowledges the open research fund of Key Laboratory of Quantum Materials and Devices (Southeast University), Ministry of Education, the National Natural Science Foundation of China (NSFC) grant 12474081, and the Start-up Research Fund of Southeast University. M.A. acknowledges the support of the National Science Foundation under Grant DMR-2329111. S.H., M. Z, R.R., J.M.L, and L.W.M. acknowledge that the research was sponsored by the Army Research Laboratory and was accomplished under Cooperative Agreement Number W911NF-24-2-0100. C.-C.L. acknowledges the support of the Army Research Office under Grant W911NF-21-1-0118. E.B., A.S., F.R., and J.B.N acknowledge the support of the U.S. Department of Energy, Office of Science, Office of Basic Energy Sciences, Materials Sciences and Engineering Division under Contract No. DE-AC02-05-CH11231 (Materials Project program KC23MP) for the development of functional materials. B.R.D. acknowledges the support of the National Science Foundation Graduate Research Fellowship under Grant No. 2141064. S.W. acknowledges the support of the U.S. Department of Energy, Office of Science, Office of Basic Energy Sciences, Materials Sciences and Engineering Division under contract No. DEAC02-05-CH11231 (EMAT program KC1201). T.Y.K. acknowledges the support of the Army Research Office under Grant W911NF-21-1-0126. L.C. acknowledges support from the National Science Foundation EPSCoR Program RII Track-4 under Grant OIA-2327352. S.H. and R.R. acknowledge the U.S. Department of Energy, Office of Science, Office of Basic Energy Sciences, Materials Sciences and Engineering Division under Contract No. DE-AC02-05-CH11231 (Codesign of Ultra-Low-Voltage Beyond CMOS Microelectronics) for the development of materials for low-power microelectronics. I.H. and R.R. acknowledge the Air Force Office of Scientific Research 2D Materials and Devices Research program through Clarkson Aerospace Corp. under Grant No. FA9550-21-1-0460. P.B. and R.R. acknowledge the support of the Army Research Office under the ETHOS MURI via cooperative agreement W911NF-21-2-0162. D.N., R.R., and L.W.M. additionally acknowledge the National Science Foundation via Grant DMR-2329111. J.M.R. acknowledges the National Science Foundation (NSF) under Grant DMR-2104397. Work at the Molecular Foundry was supported by the Office of Science, Office of Basic Energy Sciences, of the U.S. Department of Energy under Contract No. DE-AC02-05CH11231. This work was also conducted in part using resources of the Shared Equipment Authority at Rice University. The views and conclusions contained in this document are those of the authors and should not be interpreted as representing the official policies, either expressed or implied, of the Army Research Laboratory or the U.S. Government. The U.S. Government is authorized to reproduce and distribute reprints for Government purposes, notwithstanding any copyright notation herein.

Conflict of Interest

The authors declare no conflict of interest.

Data Availability Statement

Research data are not shared.

Keywords

density functional theory, epitaxy, magnetotransport, Rashba coupling, spintronics

Received: March 9, 2025
Revised: June 17, 2025
Published online:

[1] D. Xiao, M.-C. Chang, Q. Niu, *Rev. Mod. Phys.* **2010**, *82*, 1959.
[2] S. Picozzi, *AIP Conf. Proc.* **2014**, *2*, 10.
[3] A. Manchon, H. C. Koo, J. Nitta, S. M. Frolov, R. A. Duine, *Nat. Mater.* **2015**, *14*, 871.
[4] A. Soumyanarayanan, N. Reyren, A. Fert, C. Panagopoulos, *Nature* **2016**, *539*, 509.
[5] G. Bihlmayer, P. Noël, D. V. Vyalikh, E. V. Chulkov, A. Manchon, *Nat. Rev. Phys.* **2022**, *4*, 642.
[6] H. Murakawa, M. S. Bahramy, M. Tokunaga, Y. Kohama, C. Bell, Y. Kaneko, N. Nagaosa, H. Y. Hwang, Y. Tokura, *Science* **2013**, *342*, 1490.
[7] T. Ideue, K. Hamamoto, S. Koshikawa, M. Ezawa, S. Shimizu, Y. Kaneko, Y. Tokura, N. Nagaosa, Y. Iwasa, *Nat. Phys.* **2017**, *13*, 578.
[8] R. Yoshimi, K. Yasuda, A. Tsukazaki, K. S. Takahashi, M. Kawasaki, Y. Tokura, *Sci. Adv.* **2018**, *4*, aat9989.
[9] D. Choe, M.-J. Jin, S.-I. Kim, H.-J. Choi, J. Jo, I. Oh, J. Park, H. Jin, H. C. Koo, B.-C. Min, S. Hong, H.-W. Lee, S.-H. Baek, J.-W. Yoo, *Nat. Commun.* **2019**, *10*, 4510.
[10] P. Noël, F. Trier, L. M. V. Arche, J. Bréhin, D. C. Vaz, V. Garcia, S. Fusil, A. Barthélémy, L. Vila, M. Bibes, J.-P. Attané, *Nature* **2020**, *580*, 483.
[11] J. Jeon, S. W. Cho, O. Lee, J. Hong, J. Y. Kwak, S. Han, S. Jung, Y. Kim, H.-W. Ko, S. Lee, K.-J. Lee, H. C. Koo, *NPG Asia Mater* **2021**, *13*, 76.
[12] A. L. Edgeton, I. A. Harris, N. G. Campbell, Y. Chai, M. M. Mazur, G. Gurung, X. Huang, S. Susarla, E. Y. Tsymbal, D. C. Ralph, T. Nan, M. S. Rzchowski, R. Ramesh, C.-B. Eom, *Nat. Electron.* **2023**, *6*, 973.
[13] J. B. Miller, D. M. Zumbühl, C. M. Marcus, Y. B. Lyanda-Geller, D. Goldhaber-Gordon, K. Campman, A. C. Gossard, *Phys. Rev. Lett.* **2003**, *90*, 076807.
[14] S. Takasuna, J. Shiogai, S. Matsuzaka, M. Kohda, Y. Oyama, J. Nitta, *Phys. Rev. B* **2017**, *96*, 161303.
[15] F. Passmann, A. D. Bristow, J. N. Moore, G. Yusa, T. Mano, T. Noda, M. Betz, S. Anghel, *Phys. Rev. B* **2019**, *99*, 125404.
[16] A. D. Caviglia, M. Gabay, S. Gariglio, N. Reyren, C. Cancellieri, J.-M. Triscone, *Phys. Rev. Lett.* **2010**, *104*, 126803.
[17] Q. Song, H. Zhang, T. Su, W. Yuan, Y. Chen, W. Xing, J. Shi, J. Sun, W. Han, *Sci. Adv.* **2017**, *3*, 1602312.
[18] W. Lin, L. Li, F. Doğan, C. Li, H. Rotella, X. Yu, B. Zhang, Y. Li, W. S. Lew, S. Wang, W. Prellier, S. J. Pennycook, J. Chen, Z. Zhong, A. Manchon, T. Wu, *Nat. Commun.* **2019**, *10*, 3052.

[19] D. C. Vaz, F. Trier, A. Dyrdał, A. Johansson, K. Garcia, A. Barthélémy, I. Mertig, J. Barnaś, A. Fert, M. Bibes, *Phys. Rev. Mater.* **2020**, *4*, 071001.
[20] M. I. Dyakonov, V. I. Perel, *Phys. Lett. A* **1971**, *35*, 459.
[21] Y. Ohno, R. Terauchi, T. Adachi, F. Matsukura, H. Ohno, *Phys. Rev. Lett.* **1999**, *83*, 4196.
[22] P. Boross, B. Dóra, A. Kiss, F. Simon, *Sci Rep-uk* **2013**, *3*, 3233.
[23] M. P. Walser, C. Reichl, W. Wegscheider, G. Salis, *Nat. Phys.* **2012**, *8*, 757.
[24] M. Kohda, V. Lechner, Y. Kunihashi, T. Dollinger, P. Olbrich, C. Schönhuber, I. Caspers, V. V. Bel'kov, L. E. Golub, D. Weiss, K. Richter, J. Nitta, S. D. Ganichev, *Phys. Rev. B* **2012**, *86*, 081306.
[25] F. Dettwiler, J. Fu, S. Mack, P. J. Weigele, J. C. Egues, D. D. Awschalom, D. M. Zumbühl, *Phys. Rev. X* **2017**, *7*, 031010.
[26] N. Yang, G. Gou, X. Lu, Y. Hao, *Nano Res.* **2022**, *15*, 6779.
[27] J. D. Koralek, C. P. Weber, J. Orenstein, B. A. Bernevig, S.-C. Zhang, S. Mack, D. D. Awschalom, *Nature* **2009**, *458*, 610.
[28] K. Yoshizumi, A. Sasaki, M. Kohda, J. Nitta, *Appl. Phys. Lett.* **2016**, *108*, 132402.
[29] D. D. Sante, P. Barone, R. Bertacco, S. Picozzi, *Adv. Mater.* **2013**, *25*, 509.
[30] H. Wang, P. Gopal, S. Picozzi, S. Curtarolo, M. B. Nardelli, J. Sławińska, *npj Comput. Mater.* **2020**, *6*, 7.
[31] Y. Li, Y. Li, P. Li, B. Fang, X. Yang, Y. Wen, D. Zheng, C. Zhang, X. He, A. Manchon, Z.-H. Cheng, X. Zhang, *Nat. Commun.* **2021**, *12*, 540.
[32] H. Ryu, J.-M. Lihm, J. Cha, B. Kim, B. S. Kim, W. Kyung, I. Song, Y. Kim, G. Han, J. Denlinger, I. Chung, C.-H. Park, S. R. Park, C. Kim, *Phys. Rev. B* **2021**, *103*, 245113.
[33] R. Yoshimi, M. Kawamura, K. Yasuda, A. Tsukazaki, K. S. Takahashi, M. Kawasaki, Y. Tokura, *Phys. Rev. B* **2022**, *106*, 115202.
[34] H. Maaß, H. Bentmann, C. Seibel, C. Tusche, S. V. Eremeev, T. R. F. Peixoto, O. E. Tereshchenko, K. A. Kokh, E. V. Chulkov, J. Kirschner, F. Reinert, *Nat. Commun.* **2016**, *7*, 11621.
[35] M. S. Bahramy, N. Ogawa, *Adv. Mater.* **2017**, *29*, 1605911.
[36] L. L. Tao, E. Y. Tsymbal, *Nat. Commun.* **2018**, *9*, 2763.
[37] X.-Z. Lu, J. M. Rondinelli, *Matter* **2020**, *3*, 1211.
[38] L. Zhang, J. Jiang, C. Multunas, C. Ming, Z. Chen, Y. Hu, Z. Lu, S. Pendse, R. Jia, M. Chandra, Y.-Y. Sun, T.-M. Lu, Y. Ping, R. Sundararaman, J. Shi, *Nat. Photonics* **2022**, *16*, 529.
[39] M. Acharya, S. Mack, A. Fernandez, J. Kim, H. Wang, K. Eriguchi, D. Meyers, V. Gopalan, J. Neaton, L. W. Martin, *Chem. Mater.* **2020**, *32*, 7274.
[40] A. Dhingra, D. Sando, P.-S. Lu, Z. G. Marzouk, V. Nagarajan, P. A. Dowben, *J. Appl. Phys.* **2021**, *130*, 025304.
[41] Y.-H. Chu, Q. He, C.-H. Yang, P. Yu, L. W. Martin, P. Shafer, R. Ramesh, *Nano Lett.* **2009**, *9*, 1726.
[42] H. D. Megaw, C. N. W. Darlington, *Acta Crystallogr Sect Cryst Phys Diffr Theor Gen Crystallogr* **1975**, *31*, 161.
[43] A. A. Belik, T. Furubayashi, H. Yusa, E. Takayama-Muromachi, *J. Am. Chem. Soc.* **2011**, *133*, 9405.
[44] Y. Inaguma, M. Yoshida, T. Katsumata, *J. Am. Chem. Soc.* **2008**, *130*, 6704.
[45] K. Fujiwara, H. Minato, J. Shiogai, A. Kumamoto, N. Shibata, A. Tsukazaki, *APL Mater.* **2019**, *7*, 022505.
[46] Y. Inaguma, A. Aimi, D. Mori, T. Katsumata, M. Ohtake, M. Nakayama, M. Yonemura, *Inorg. Chem.* **2018**, *57*, 15462.
[47] S. Lanfredi, A. C. M. Rodrigues, *J. Appl. Phys.* **1999**, *86*, 2215.
[48] R. Xu, J. Karthik, A. R. Damodaran, L. W. Martin, *Nat. Commun.* **2014**, *5*, 3120.
[49] M. Acharya, D. Lou, A. Fernandez, J. Kim, Z. Tian, L. W. Martin, *Phys. Rev. Appl.* **2023**, *20*, 014017.
[50] X.-Z. Lu, J. M. Rondinelli, *Phys. Rev. B* **2023**, *107*, 035155.
[51] T. Koga, J. Nitta, T. Akazaki, H. Takayanagi, *Phys. Rev. Lett.* **2002**, *89*, 046801.
[52] L. Li, Y. Wu, X. Liu, J. Liu, H. Ruan, Z. Zhi, Y. Zhang, P. Huang, Y. Ji, C. Tang, Y. Yang, R. Che, X. Kou, *Adv. Mater.* **2023**, *35*, 2207322.
[53] T. Nihei, Y. Suzuki, M. Kohda, J. Nitta, *Phys. Status Solidi C* **2007**, *3*, 4239.
[54] D. Spirito, L. D. Gaspare, F. Evangelisti, A. D. Gaspare, E. Giovine, A. Notargiacomo, *Phys. Rev. B* **2012**, *85*, 235314.
[55] W. Knap, C. Skierbiszewski, A. Zduniak, E. Litwin-Staszewska, D. Bertho, F. Kobbi, J. L. Robert, G. E. Pikus, F. G. Pikus, S. V. Iordanskii, V. Mosser, K. Zekentes, Y. B. Lyanda-Geller, *Phys. Rev. B* **1996**, *53*, 3912.
[56] H. Fukuyama, K. Hoshino, *J. Phys. Soc. Jpn.* **1981**, *50*, 2131.
[57] A. A. Taskin, H. F. Legg, F. Yang, S. Sasaki, Y. Kanai, K. Matsumoto, A. Rosch, Y. Ando, *Nat. Commun.* **2017**, *8*, 1340.
[58] N. Wadehra, R. Tomar, R. M. Varma, R. K. Gopal, Y. Singh, S. Dattagupta, S. Chakraverty, *Nat. Commun.* **2020**, *11*, 874.
[59] T. Guillet, C. Zucchetti, Q. Barbedienne, A. Marty, G. Isella, L. Cagnon, C. Vergnaud, H. Jaffrès, N. Reyren, J.-M. George, A. Fert, M. Jamet, *Phys. Rev. Lett.* **2020**, *124*, 027201.
[60] N. Roschewsky, E. S. Walker, P. Gowtham, S. Muschinske, F. Hellman, S. R. Bank, S. Salahuddin, *Phys. Rev. B* **2019**, *99*, 195103.
[61] K. Premasiri, S. K. Radha, S. Sucharitakul, U. R. Kumar, R. Sankar, F.-C. Chou, Y.-T. Chen, X. P. A. Gao, *Nano Lett.* **2018**, *18*, 4403.
[62] G. Kresse, J. Hafner, *Phys. Rev. B* **1993**, *47*, 558.
[63] G. Kresse, J. Furthmüller, *Comput. Mater. Sci.* **1996**, *6*, 15.
[64] G. Kresse, J. Furthmüller, *Phys. Rev. B* **1996**, *54*, 11169.
[65] G. Kresse, D. Joubert, *Phys. Rev. B* **1998**, *59*, 1758.
[66] P. A. M. Dirac, *Math. Proc. Camb. Philos. Soc.* **1930**, *26*, 376.
[67] D. M. Ceperley, B. J. Alder, *Phys. Rev. Lett.* **1980**, *45*, 566.
[68] J. P. Perdew, A. Zunger, *Phys. Rev. B* **1981**, *23*, 5048.
[69] J. P. Perdew, K. Burke, M. Ernzerhof, *Phys. Rev. Lett.* **1996**, *77*, 3865.
[70] J. P. Perdew, A. Ruzsinszky, G. I. Csonka, O. A. Vydrov, G. E. Scuseria, L. A. Constantin, X. Zhou, K. Burke, *Phys. Rev. Lett.* **2008**, *100*, 136406.
[71] J. W. Furness, A. D. Kaplan, J. Ning, J. P. Perdew, J. Sun, *J. Phys. Chem. Lett.* **2020**, *11*, 8208.
[72] R. Kingsbury, A. S. Gupta, C. J. Bartel, J. M. Munro, S. Dwaraknath, M. Horton, K. A. Persson, *Phys. Rev. Mater.* **2022**, *6*, 013801.
[73] J. Sun, A. Ruzsinszky, J. P. Perdew, *Phys. Rev. Lett.* **2015**, *115*, 036402.
[74] J. Sun, R. C. Remsing, Y. Zhang, Z. Sun, A. Ruzsinszky, H. Peng, Z. Yang, A. Paul, U. Waghmare, X. Wu, M. L. Klein, J. P. Perdew, *Nat. Chem.* **2016**, *8*, 831.
[75] S. P. Ong, L. Wang, B. Kang, G. Ceder, *Chem. Mater.* **2008**, *20*, 1798.
[76] T. E. Smidt, S. A. Mack, S. E. Reyes-Lillo, A. Jain, J. B. Neaton, *Sci. Data* **2020**, *7*, 72.
[77] C. Capillas, E. S. Tasci, G. de la Flor, D. Orobengoa, J. M. Perez-Mato, M. I. Aroyo, *Z. für Krist.* **2011**, *226*, 186.
[78] F. Ricci, S. E. Reyes-Lillo, S. A. Mack, J. B. Neaton, *npj Comput. Mater.* **2024**, *10*, 15.
[79] P. E. Blöchl, *Phys. Rev. B* **1994**, *50*, 17953.
[80] J. Bardeen, *J. Chem. Phys.* **1938**, *6*, 367.
[81] F. Seitz, R. P. Johnson, *J. Appl. Phys.* **1937**, *8*, 186.